Article

Cell

The Architecture of Talin1 Reveals an Autoinhibition Mechanism

Graphical Abstract

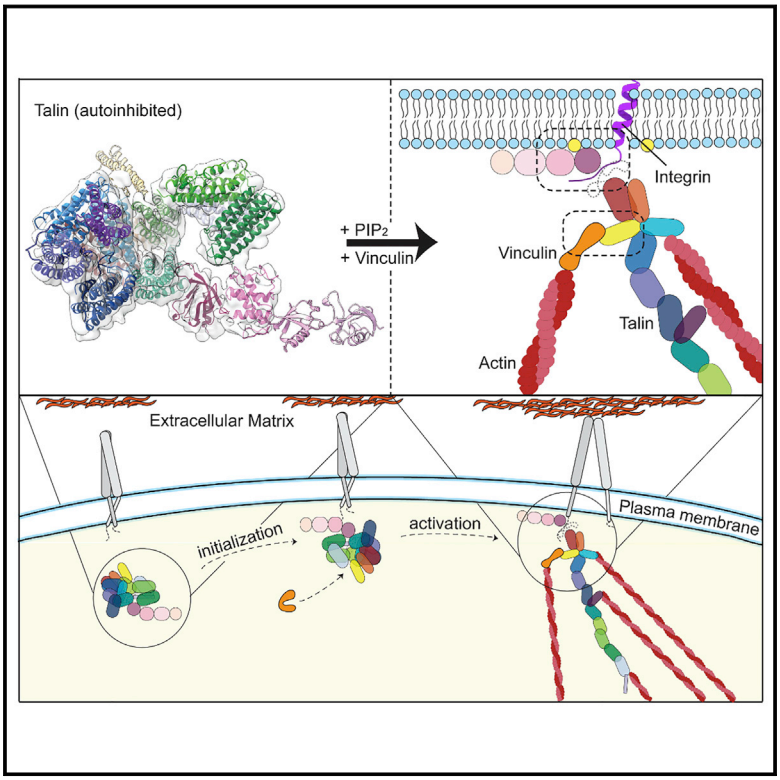

Authors

Dirk Dedden, Stephanie Schumacher, Charlotte F. Kelley, Martin Zacharias, Christian Biertümpfel, Reinhard Fässler, Naoko Mizuno

Correspondence

mizuno@biochem.mpg.de

In Brief

Structural characterization of talin shows how autoinhibition regulates interactions crucial for cell-cell contact and tension sensing.

Highlights

- The structure of the autoinhibited human full-length talin1 was analyzed by cryo-EM
- Talin1 reversibly changes between a 15-nm closed and a ~60-nm open conformation
- Rod R9/R12 and FERM domains synchronously shield membrane and cytoskeleton binding
- F-Actin and vinculin binding to talin is regulated by the opening of talin

Dedden et al., 2019, Cell *179*, 120–131
September 19, 2019
https://doi.org/10.1016/j.cell.2019.08.034

CellPress

Cell

Article

The Architecture of Talin1 Reveals an Autoinhibition Mechanism

Dirk Dedden,[1] Stephanie Schumacher,[1] Charlotte F. Kelley,[1] Martin Zacharias,[2] Christian Biertümpfel,[1] Reinhard Fässler,[3] and Naoko Mizuno[1,4,*]

[1]Department of Structural Cell Biology, Max Planck Institute of Biochemistry, Am Klopferspitz 18, 82152 Martinsried, Germany
[2]Physics Department (T38), Technical University Munich, James-Franck-Str. 1, 85748 Garching, Germany
[3]Department of Molecular Medicine, Max Planck Institute of Biochemistry, Am Klopferspitz 18, 82152 Martinsried, Germany
[4]Lead Contact
*Correspondence: mizuno@biochem.mpg.de
https://doi.org/10.1016/j.cell.2019.08.034

SUMMARY

Focal adhesions (FAs) are protein machineries essential for cell adhesion, migration, and differentiation. Talin is an integrin-activating and tension-sensing FA component directly connecting integrins in the plasma membrane with the actomyosin cytoskeleton. To understand how talin function is regulated, we determined a cryoelectron microscopy (cryo-EM) structure of full-length talin1 revealing a two-way mode of autoinhibition. The actin-binding rod domains fold into a 15-nm globular arrangement that is interlocked by the integrin-binding FERM head. In turn, the rod domains R9 and R12 shield access of the FERM domain to integrin and the phospholipid PIP_2 at the membrane. This mechanism likely ensures synchronous inhibition of integrin, membrane, and cytoskeleton binding. We also demonstrate that compacted talin1 reversibly unfolds to an ~60-nm string-like conformation, revealing interaction sites for vinculin and actin. Our data explain how fast switching between active and inactive conformations of talin could regulate FA turnover, a process critical for cell adhesion and signaling.

INTRODUCTION

Focal adhesions (FAs) are intracellular protein assemblies that serve as tension-sensing anchoring points to link cells to the extracellular environment (Geiger et al., 2009; Parsons et al., 2010). FAs not only tether cells to the extracellular matrix (ECM), but also facilitate intracellular reorganization, resulting in dynamic changes in cell functions and cell morphologies (Geiger et al., 2009; Legate et al., 2009; Parsons et al., 2010). FAs consist of hundreds of proteins in a layered arrangement that closely regulate each other (Kanchanawong et al., 2010). The first layer consists of integrin-signaling components at the plasma membrane, the second of force-transduction components, the third of actin-regulatory factors, and the fourth layer is made up of actin fibers. Several key proteins act to coordinate the individual functions of each layer, mediate crosstalk between layers, and to connect these layers with integrin receptor, the master-controller that links cytoplasmic FA complexes to the ECM (Bachir et al., 2014).

FA-mediated cellular processes are facilitated by alternating states of active and inactive integrins. In migrating cells, integrin activation initiates vast FA formation, allowing cells to attach to the extracellular environment, whereas integrin inactivation, followed by disassembly of FAs, detaches cells. This cycling of on/off states allows cells to continuously change anchoring points, facilitating cellular movement. Talin is a key component in FAs, responsible for activating integrins and mediating both inside-out and outside-in signaling (Tadokoro et al., 2003; Harburger and Calderwood, 2009; Nieswandt et al., 2007). Talin activates integrin by associating with the cytosolic tail of integrin beta-subunits. Once engaged, talin can assume an elongated conformation up to 100 nm in length (Liu et al., 2015), directly linking the beta-integrin subunit in the first layer of the FA to actin bundles in the fourth layer (Kanchanawong et al., 2010). By spanning all four layers of the FA, talin is in a unique position to act as a structural scaffold, greatly contributing to the overall composition and organization of FA complexes (Calderwood et al., 2013). In addition to its role as an integrin activator, talin also acts as a mechanosensor; it stretches like a spring and transmits tension between the ECM and the actomyosin machinery within the FA (Austen et al., 2015; Kumar et al., 2016), a process which is essential for regulating FA maturation and stability. As such, the transition between active and inactive talin likely plays a key regulatory role in FA dynamics, similar to the activation and inactivation of integrins.

Talin is a large, 270 kDa protein with 18 domains comprising an ~50 kDa globular head, a long rod made of 62 helices forming 13 helical bundle (rod) domains (R1–R13) (Calderwood et al., 2013; Goult et al., 2013), and a dimerization (DD) motif at the C terminus (Gingras et al., 2008). A unique conformational change of talin facilitates its spring-like behavior, through which talin can unfold into a linearly elongated 60–100 nm rod-like shape (Liu et al., 2015; Molony et al., 1987; Winkler et al., 1997). This allows it to bind to at least 11 different FA components including vinculin and actin (Goult et al., 2018). The talin head contains a 4.1-ezrin-radixin-moesin (FERM) domain with four subdomains (F0–F3), which is a common structural feature of several integrin tail-binding proteins (Elliott et al., 2010; Garcia-Alvarez et al., 2003; Goult et al., 2010; Rees et al., 1990). The FERM domain contains the integrin-binding site IBS1 (Tanentzapf and Brown, 2006; Wegener et al., 2007) and phosphatidylinositol-4,5-bisphosphate (PIP_2)

recognition site, allowing talin to attach to the membrane surface in a regulated way. The force-mediated stretching of talin is thought to follow (Atherton et al., 2015; Margadant et al., 2011), resulting in the exposure of up to 11 cryptic binding sites for vinculin (Fillingham et al., 2005; Gingras et al., 2005; Izard et al., 2004; Papagrigoriou et al., 2004). The binding of vinculin to talin is proposed to reinforce FA strength, as vinculin facilitates binding to actin, resulting in a cable-like configuration of F-actin (Case et al., 2015; Kanchanawong et al., 2010; Liu et al., 2015; Carisey et al., 2013; Humphries et al., 2007) and triggering the maturation of the FA (Zaidel-Bar et al., 2003).

While the active form of talin is well-characterized, the critical state of the inhibited form of talin is scarcely understood. The importance of talin inhibition is highlighted by the fact that disruption of proper talin inhibition leads to morphogenetic defects during fly development (Ellis et al., 2013) and it has been implicated in the migration of metastatic cancer cells (Desiniotis and Kyprianou, 2011; Fang et al., 2016; Haining et al., 2016). In its autoinhibited state, talin has a compact conformation (Goldmann et al., 1994; Goult et al., 2013; Winkler et al., 1997), with domains folded into each other, to occlude the interaction sites for binding partners such as integrin, membrane, vinculin, and F-actin. Although individual, truncated fragments of talin have been well-characterized, the regulation of full-length talin and the interplay among its domains are largely unknown on a molecular level. For example, a truncated fragment of the FERM domain (F3) was shown to interact with the R9 rod domain (Song et al., 2012); however, the overall mechanism is unclear because of the lack of information about the full-length architecture of talin.

Here, we report a cryoelectron microscopy (cryo-EM) structure of the autoinhibited form of recombinantly produced full-length talin1. The structure reveals charge-based interactions among the 13 rod domains of the talin1 monomer that entangle the protein into a compact 15 nm globular architecture, which is further secured by respective interactions between the F2 and F3 FERM subdomains and the R12 and R9 rod domains. Interestingly, the PIP_2-binding surface of the FERM domain is completely covered by the rod domain R12 to occlude access to the plasma membrane. The integrin-binding site is located at the deepest part of the autoinhibition pocket. The closure of the rod domains impedes binding to vinculin and to actin via the actin-binding site 2 (ABS2), although it does not occlude the other actin-binding site, ABS3. By mimicking talin activation, we facilitated talin1 binding to F-actin and vinculin. On the basis of these results, we propose a molecular model that explains how talin activation is controlled at a PIP_2-enriched membrane surface and how the protein transitions from a 15 nm globular structure to a 100 nm extended structure. Our results have wide-ranging implications for the mechanistic understanding of FAs and protein activation.

RESULTS

The Full-Length, Autoinhibited Talin1 Structure Shows Molecular Closure of the Rod Domains by the FERM Domain

Talin is thought to adopt open and closed conformational states (Figure 1A). While open talin is amenable to further stretching by its interacting partners, the globular state is likely to take on an autoinhibited conformation that hinders access to many of talin's binding sites, restricting interactions with other FA proteins. The autoinhibited form is thought to be the cytosolic state of talin that does not engage in FA assembly. It has been a challenge, however, to obtain a molecular view of the autoinhibited conformation. We successfully purified recombinantly expressed talin1 and pursued a full structural and biochemical characterization.

The cryo-EM analysis of full-length talin1 (talin-FL) in the autoinhibited conformation (Figures 1B, S1, and S2; Table S1) revealed an intertwined architecture. Although the intrinsic flexibility of talin limited the resolution of the structural reconstruction to a global resolution of 6.2 Å (Figures S2A–S2C; Table S1), the clear connectivity of the rod domains within the density map facilitated robust fitting of available structures of the 13 individual rod domains and the F2 and F3 subdomains of the FERM domain (Figures 1C and S3). We performed further refinement using a flexible fitting scheme by restraint molecular dynamics (Salomon-Ferrer et al., 2013). Our results show that the rod domains are entangled with each other, resulting in a compact organization, and the FERM domain closes the assembly via two anchoring points on rod domains R9 and R12, respectively, acting as a lid to secure the closure of the talin architecture (Figure 1D). At the first anchoring point, located in the deepest groove of the autoinhibition pocket (Figure 1E), the interacting surface between R9 and F3 agrees well with a previously reported crystal structure of isolated F3 and R9 fragments (Song et al., 2012) (Figure S4), which are necessary for talin inhibition in cells. At the second anchoring point (Figure 1E), located at the critical connecting point for the closure of talin1, K272 and K274 in F2 contact E2288 and D2297 at the C terminus of R12, respectively (Figure 1D).

While the F2 and F3 FERM subdomains revealed interactions necessary for talin1 autoinhibition, the densities corresponding to the F0 and F1 FERM subdomains were not visualized in our structure (Figure 1E). F0 serves as an interaction surface for the small GTPase Rap1 (Zhu et al., 2017), which acts as a recruiting factor to promote talin engagement with the plasma membrane (Goult et al., 2010; Plak et al., 2016) (Figure 1F). While these subdomains are missing from our structure, the corresponding fragments were identified by mass spectrometry (Figure S3B). This indicates that the F0-F1 subdomains are flexibly attached to the talin core structure, presumably by a long, 30 amino-acid linker between F1 and F2 (Figure 1E). Hence, F0 and F1 are likely not part of the inhibited structure, which suggests that talin can be recruited to the membrane surface via Rap1 without requiring disentanglement of the rod domains or disruption of the FERM domain interaction with R9 and R12 (Figures 1E and 1F).

The Closed Talin Configuration Occludes the Integrin-Binding Site and the Membrane-Binding Surface on the FERM Domain

The talin FERM domain was shown to interact with PIP_2 (Chinthalapudi et al., 2018; Orłowski et al., 2015; Song et al., 2012). Specific residues responsible for this interaction were recently identified including K272 of F2 and K316, K324, E342, and K343 of F3 (Chinthalapudi et al., 2018). We mapped their

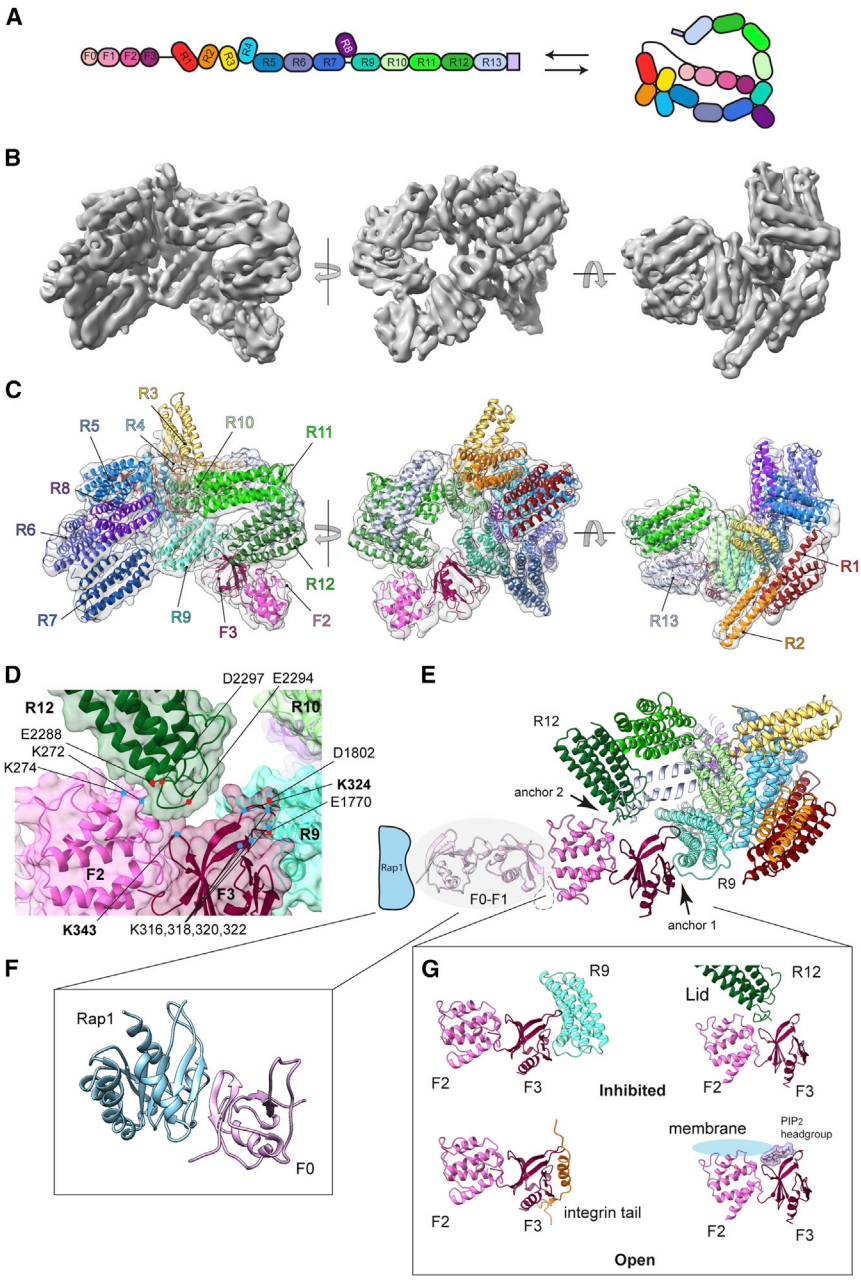

Figure 1. Structure of Full-Length Talin

(A) Schematic of the domain organization of talin in the open form (left) and the closed, autoinhibited form (right).

(B) Three views of the structure of full-length talin.

(C) Molecular fitting of talin fragments (PDB: 3IVF, 1SJ8, 2L7A, 2LQG, 2L7N, 2L10, 5IC1, 2KVP, 3DYJ, and 2JSW) to the EM density map.

(D) The molecular closure of talin achieved by F2-R12 and F3-R9 interactions and the charged amino acids surrounding the interaction interface. Bold highlighted numbers match previously published PIP_2-recognition residues.

(E) Superimposition of the F0-F1 subdomains of the talin FERM domain structure (overlaid with grey shadow, PDB: 3IVF) onto our cryo-EM talin model. The F0 and F1 subdomains were not visualized in our structural analysis due to the flexibility of the F1-F2 linker. The small GTP Rap1-binding site on F0 is mapped in blue and labelled "Rap1."

(F) The NMR structure of F0-Rap1 (PDB: 6BA6).

(G) Comparison of the F3-R9 and F2-R12 auto-inhibition sites in the closed structure with the F3-integrin tail (PDB: 2H7D) and F2-F3-PIP_2 (PDB: 6MFS) as well as with the membrane-interaction sites of the FERM domain (Anthis et al., 2009), highlighting the mechanism of the autoinhibition of talin. In the inhibited form R12 forms a "lid" covering the PIP_2-binding site on F2-F3.

See also Figures S1, S2, S3, S4, and S5 and Table S1.

locations to understand the geometrical relationships among them in full-length talin (Figure 1D). In the autoinhibited talin structure, the PIP_2-binding surface was mostly covered by the rod domains, particularly by a region at the C terminus of R12, ensuring that the binding site was inaccessible to PIP_2 (Figures 1D and 1G). This region, containing the negatively charged amino acids E2288, E2294, and D2297 (Figure 1D), provides an acidic interface to complement the basic PIP_2-binding surface. Furthermore, to understand the arrangement of integrin and the plasma membrane with respect to talin in the open and closed configurations, we superimposed the available structure of the integrin cytosolic tail in complex with F3 (Anthis et al., 2009; Wegener et al., 2007) (Figure 1G). The integrin tail was shown to bind on the surface of the truncated F3 (Song et al., 2012), where R9 also binds in our autoinhibited structure, showing that the integrin-F3 interaction and the F3-R9 autoinhibitory interaction are mutually exclusive. Moreover, the integrin transmembrane helix directly precedes the integrin tail, indicating that F2 and R12 would have to separate to enable F2 and F3 to bind the inner face of the plasma membrane (Figure 1G). We also noted that the interaction surface of F3 for R9 has been reported to be a key interface for talin-binding partners, such as RIAM (Yang et al., 2014) and layilin (Wegener et al., 2008), which are likely involved in talin activation (Figure S4).

The Talin1 Folding Unit Is a Monomer in the Autoinhibited Form

The last 50 amino acids at the C terminus of talin1 have been crystalized as a coiled-coil in a dimeric structure (Gingras et al., 2008) (termed DD domain), suggesting the possibility that talin is capable of dimer formation. Furthermore, talin has been separately observed as a dumbbell-shaped dimer (Goldmann et al., 1994) when interacting with actin and as entwined dimers forming a globular assembly (Goult et al., 2013), keeping

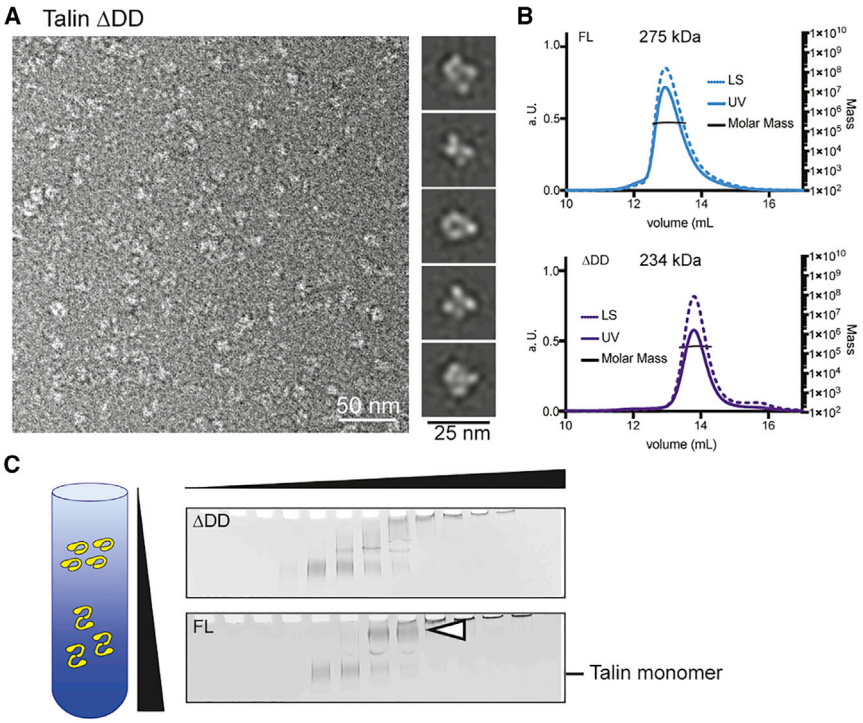

Figure 2. The Dimerization Domain Is Not Necessary for the Closure of Talin

(A) Negative-stain EM image of talin-ΔDD lacking the dimerization domain at 75 mM KCl, and 2D averages of the particles (right), showing a morphology similar to that of talin-FL.

(B) Size-exclusion chromatography coupled with multi-angle light-scattering profile of talin-FL and talin-ΔDD at 75 mM KCl, showing molecular weights corresponding to monomers. LS, light scattering, normalized; UV, absorbance.

(C) Centrifugation profiles of talin-ΔDD and talin-FL using the GraFix method. Talin-FL has an extra band in the fraction at higher sucrose density (open arrowhead). Black triangles depict the gradient of sucrose and glutaraldehyde concentrations.

the question open as to whether or not talin dimerization is necessary for its autoinhibition. Our cryo-EM structure clearly showed that talin1 monomers are capable of achieving an autoinhibited architecture.

The DD domain, which follows R13, was not clearly visible in our structure because of its flexibility, which in turn indicates that it is not engaged in the autoinhibited conformation. Indeed, a truncated talin construct that lacked the DD domain (talin-ΔDD) (Figure S3A) was still capable of assuming the autoinhibited conformation (Figure 2A), and analysis by size-exclusion chromatography coupled with multi-angle light scattering (SEC-MALS; Figure 2B) showed that both talin-FL and talin-ΔDD behave as monomers. Therefore, the DD domain appears to be inactive or not strong enough to hold talin-FL dimers together when talin is in the autoinhibited state. We further tested if we could find talin dimers as a minor component in the molecular population. Sucrose-gradient centrifugation of talin-FL in the presence of a concomitant gradient of the cross-linker glutaraldehyde (GraFix) (Stark, 2010) showed a minor population of talin that migrated differently in solution as well as on SDS-PAGE (Figure 2C), suggesting the presence of a talin-FL dimer, in agreement with the previous report (Goldmann et al., 1994). In contrast, talin-ΔDD did not display the corresponding minor band and showed only a single monomeric population, indicating that DD is the only domain in talin that is capable of facilitating dimerization.

Weak Interactions among Rod Domains Maintain the Compaction of Talin

To explore how the molecular opening of talin is regulated, we varied the ionic environment and tested if and how the conformation was changing. When we raised the ionic environment to 500 mM salt (NaCl or KCl), the conformation of full-length talin changed from the globular, closed architecture to the open, strand-like conformation (Figures 3A and 3B) with a length of 560 Å (SD = 170 Å) (Figure 3C), which fits well to the reported length of talin in a cell (Kanchanawong et al., 2010; Margadant et al., 2011). We looked for evidence of the conformational change as a function of the salt concentration using dynamic light-scattering (DLS) (Figure 3D), and the results fit well with a two-state model of protein folding-unfolding. At an ionic strength of 234 mM salt, the two states were equally populated and at a physiological salt concentration of 150 mM, 81% of talin had a compact conformation. We also found that this conformational change was reversible across fluctuating salt concentrations (Figure 3E).

Furthermore, we tested the importance of the inter-domain interactions for autoinhibition by creating point mutations as well as truncated talin constructs lacking the key domains for the interaction of F2-R12. We created a C-terminal truncation N-R11 lacking R12 and the C-terminus (Figure S3A), one of the two contact points necessary for the FERM-rod interactions, as well as N-R12 (Figure S3A). The DLS experiments showed the conformational changes of both constructs in response to the increase of salt concentration (Figure 3F). Point mutants of talin-FL altering the charge at the key interacting points on R12 (talin-FL-5K: E2288K/E2294K/D2297K/E2299K/D2300K and talin-FL-2K: E2288K/E2294K, Figure 1D) revealed a compact conformation at 75 mM salt and underwent a conformational change similar to wild type talin-FL upon change of the salt concentration (Figure 3G). These experiments led us to hypothesize that the rod domains themselves interact with each other to maintain a compact formation.

The rod domains contain several binding sites for critical FA components. Those sites include the F-actin-binding sites ABS2 and ABS3 on R4-R8 and R13-DD, respectively (Hemmings et al., 1996). We observed additional contacts among rod domains, as shown by the mapping of neighboring domains (Figure 4A). Particularly, R4 is placed at the "core" of the globular

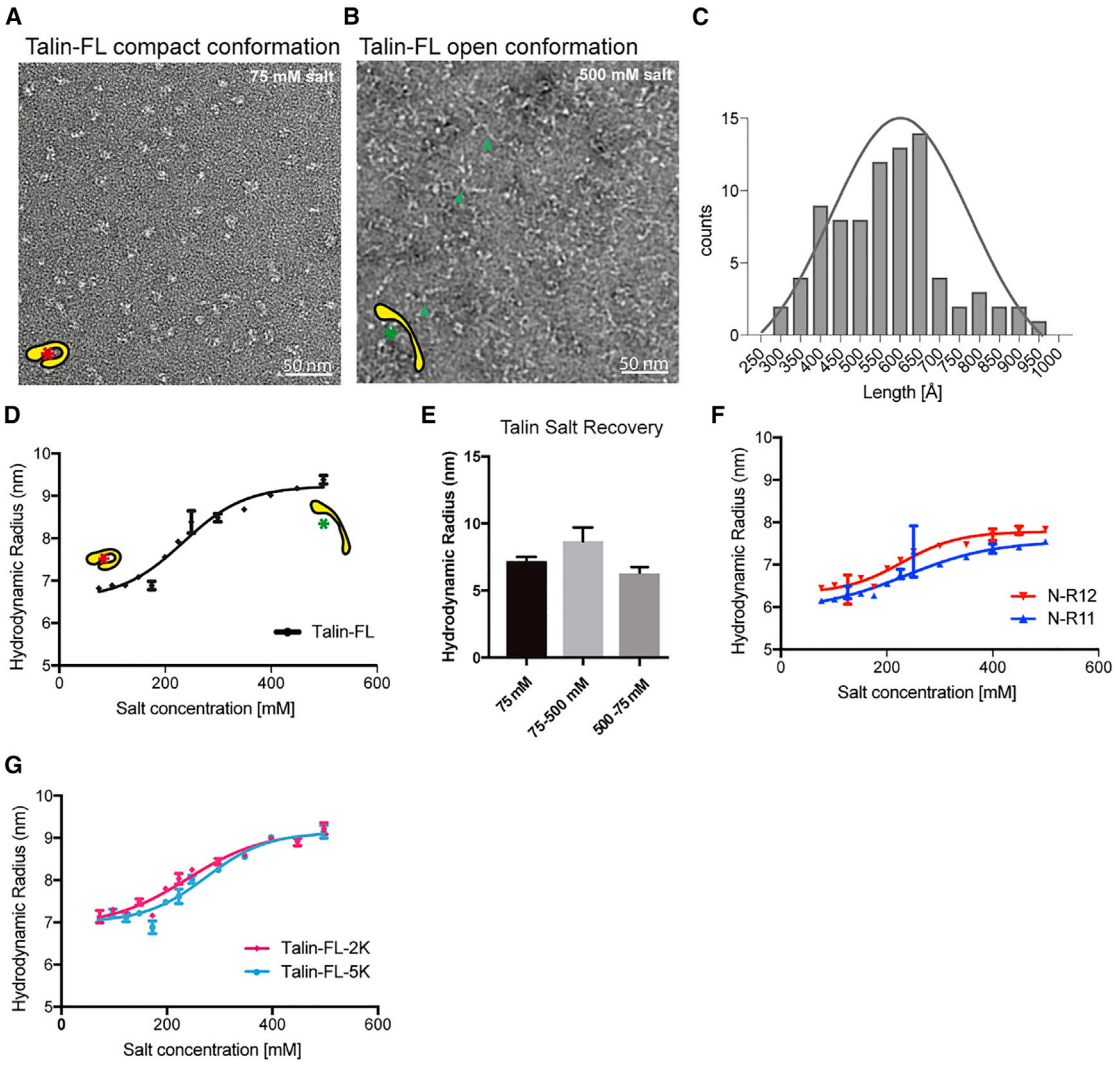

Figure 3. Two-State Conformational Ensemble of Talin

(A) Negative-stain EM image of talin-FL in the compact conformation at 75 mM KCl.

(B) Talin-FL in the open conformation in the presence of 500 mM KCl. Green arrowheads indicate examples of open talin.

(C) Distribution of the lengths of the open talin molecules from B (560 ± 170 Å, mean ± SD, N = 89).

(D) Dynamic light-scattering (DLS) measurements of the hydrodynamic radius of talin-FL under various salt concentrations, showing the conformational change of talin as a function of salt concentration. The fitted curve indicates that talin adopts both conformations at an equal ratio at a salt concentration of 234 mM. At a physiological salt concentration of 150 mM, 81% of talin employs the compact formation.

(E) Reversible conformational change of talin depending on the salt concentration as determined by DLS. Left: talin employs a closed conformation at an ionic strength of 75 mM. Center: talin opens and increases its size when the ionic strength is increased to 500 mM. Right: talin closes again when the ionic strength is lowered back to 75 mM, showing that the shape change of talin is reversible.

(F) DLS measurements of the hydrodynamic radius of N-R11 and N-R12 under various salt concentrations, showing a conformational change comparable to talin-FL with a lower amplitude. The data point at 250 mM was removed as the measurement was outside of the dynamic range of the detector.

(G) DLS measurements of point mutants of talin-FL-2K and talin-FL-5K, also showing conformational changes dependent on salt concentration. Error bars show standard deviations.

architecture and shielded by several rod domains (Figure 4B). We therefore tested the overall interactions among the rod domains by using a truncation construct that lacks the FERM domain (R1-C). DLS showed the change of the conformation in response to salt concentration (Figure 4C). To visualize the nature of the interaction, we calculated the electrostatic surface potential of each of the individual rod domains surrounding R4 and estimated the interaction energies of those domains to R4 (Figures 4A and S5). The calculated energy landscape for the domain-domain interactions indicated that the binding is rather weak (Figure S5B), resulting in an overall marginal stability. The rod domains may not rigidly bind to one another without cooperative, multi-module packing, as induced by the overall arrangement of the full-length protein. This explains the observation

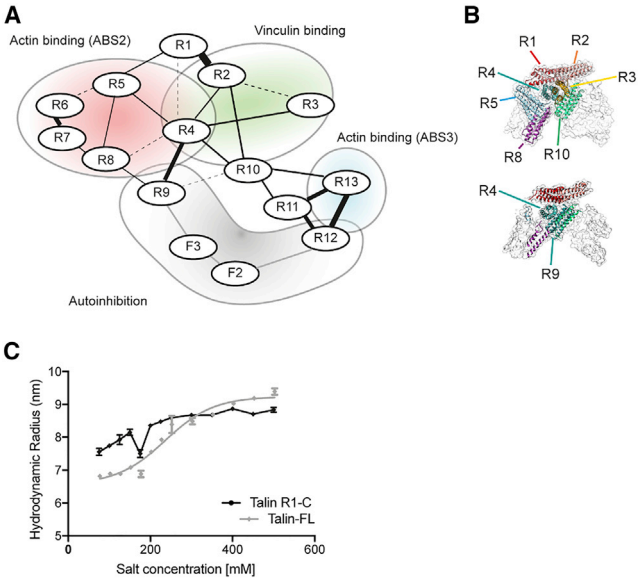

Figure 4. Interdomain Interactions of Talin

(A) Map of talin interdomain interactions derived from the EM structure. Binding domains relevant to this study are colored in red (actin-binding site ABS2), blue (actin-binding site ABS3), and green (vinculin-binding site). Dotted lines indicate positive (i.e., interactions are not favorable), while solid lines depict negative interaction energies (i.e., domains are interactive) as determined by MD simulations (see STAR Methods). The thickness of the lines is proportional to the calculated energies detailed in Figure S5.

(B) Spatial arrangement of the rod domains surrounding the R4 core in two vertical slices through the structure.

(C) DLS measurements of the hydrodynamic radius of R1-C under various salt concentrations in comparison to talin-FL (grey). The size distribution could not be fit to a two-state model. Error bars show standard deviations.

See also Figure S5.

that the talin architecture is highly sensitive and how its conformation can rapidly change in response to salt.

The Closed Conformation of Talin Prevents Vinculin Binding, whereas the Open Conformation Binds Vinculin with 1:1 Stoichiometry

Vinculin is a major talin-binding partner that facilitates crosstalk between talin and actin through its talin-binding head domain (V-head) and its actin-binding tail domain (V-tail) (Borgon et al., 2004; Johnson and Craig, 1994). Sequence-based analysis identified 11 potential vinculin-binding sites (VBSs) in talin (Gingras et al., 2005). Experiments using combinations of talin rod fragments indicated that R3, containing two VBSs, is a potent binding site for vinculin. It has been proposed that the unfolding of the helical bundle in R3 exposes the otherwise hidden binding domain to vinculin (Izard et al., 2004; Yao et al., 2014). Our truncation experiments supported that notion, as the talin fragments R1–R8 and R1–R3 formed complexes with V-head, whereas R4–R8 did not (Figure S6). It was unclear, however, how those observations would be reflected in the context of full-length talin.

To test the binding of vinculin to talin-FL, we performed reconstitution assays using size-exclusion chromatography (SEC, Figure 5A) at 75 mM KCl, where talin shows a compact architecture. While various truncations of talin including R3 readily bound to vinculin (Figure S6), the majority of talin-FL did not form complexes with full-length vinculin, V-head, or the vinculin mutant (V-mut, N773A/E775A) (Cohen et al., 2005), which exposes the talin interaction site by weakening the autoinhibition of vinculin (Figure 5A, first row). These findings suggest that the opening of the R3 helical bundle is hindered by steric constraints in the autoinhibited form of talin. The root of R3 is connected to R4, which is buried in the core of autoinhibited talin. Therefore, we attempted to reconstitute the talin-vinculin complex with talin at 500 mM KCl, where talin shows an open conformation. SEC revealed that talin and vinculin formed stable complexes with the V-mut (Figure 5A, second row). Talin formed a complex with V-head as well (Figures 5A and 5B). SEC-MALS showed that the corresponding chromatographic peaks were monodisperse with a molecular mass of 339 kDa, corresponding to a complex comprising one talin-FL and one vinculin molecule (Figure 5C). Interestingly, the talin-FL-2K and talin-FL-5K mutants, which were designed to weaken the interactions between F2 and R12 domains, were able to form a complex with V-head at 75 mM KCl (Figures 5D and 5E) significantly more than wild type talin-FL. This indicates that the disruption of F2-R12 leads to a partial access of vinculin, while these mutants employ compact conformations under this condition (Figure 3G).

The Compact Talin Can Retain Vinculin Head as a Complex but Induces the Dissociation of Full-Length Vinculin

To test the conformational change of talin in complex with vinculin, we exposed the reconstituted talin-V-head complex to low ionic strength conditions. We found that the retention volume of the SEC peak of the complex shifted from 1.27 mL (500 mM salt) to 1.31 mL (75 mM salt) (Figures 5A, S7A, and S7E), suggesting a possible compaction of the complex. DLS experiments of the preformed talin-FL-V-head complex indeed showed a conformational change upon variation in salt concentration, similar to talin-FL alone (Figures S7B–S7D). We also observed the conformational change of the complex of V-head with talin-FL-2K as well as talin-FL-5K, altogether pointing to the ability of talin to change its conformation in complex with vinculin head (Figures S7B and S7C).

The closed talin-V-head complex displayed a globular assembly that was similar to the closed morphology of talin alone (Figure S7F), although the talin-V-head complex had a slightly larger size (100 Å × 230 Å) than talin alone (~100 Å × 150 Å). Two-dimensional class averages of the talin-vinculin complex revealed a 60 Å protrusion from the ~100 Å globular head (Figure S7F, top panel). By combining available crystal structures of the talin VBS3 peptide bound to the vinculin N-terminal rods (N-terminal part of the vinculin head) (Izard et al., 2004), a full-length vinculin (Borgon et al., 2004), and our cryo-EM full-length talin in the autoinhibited form, we assembled a structural model of V-head binding to talin at the R3 domain with the talin helical bundle unfolded (Izard et al., 2004; Yao et al., 2014) (Figure S7G). This model matched well with the shape of the averaged talin-V-head complex (Figure S7F), indicating that the 60 Å protrusion on

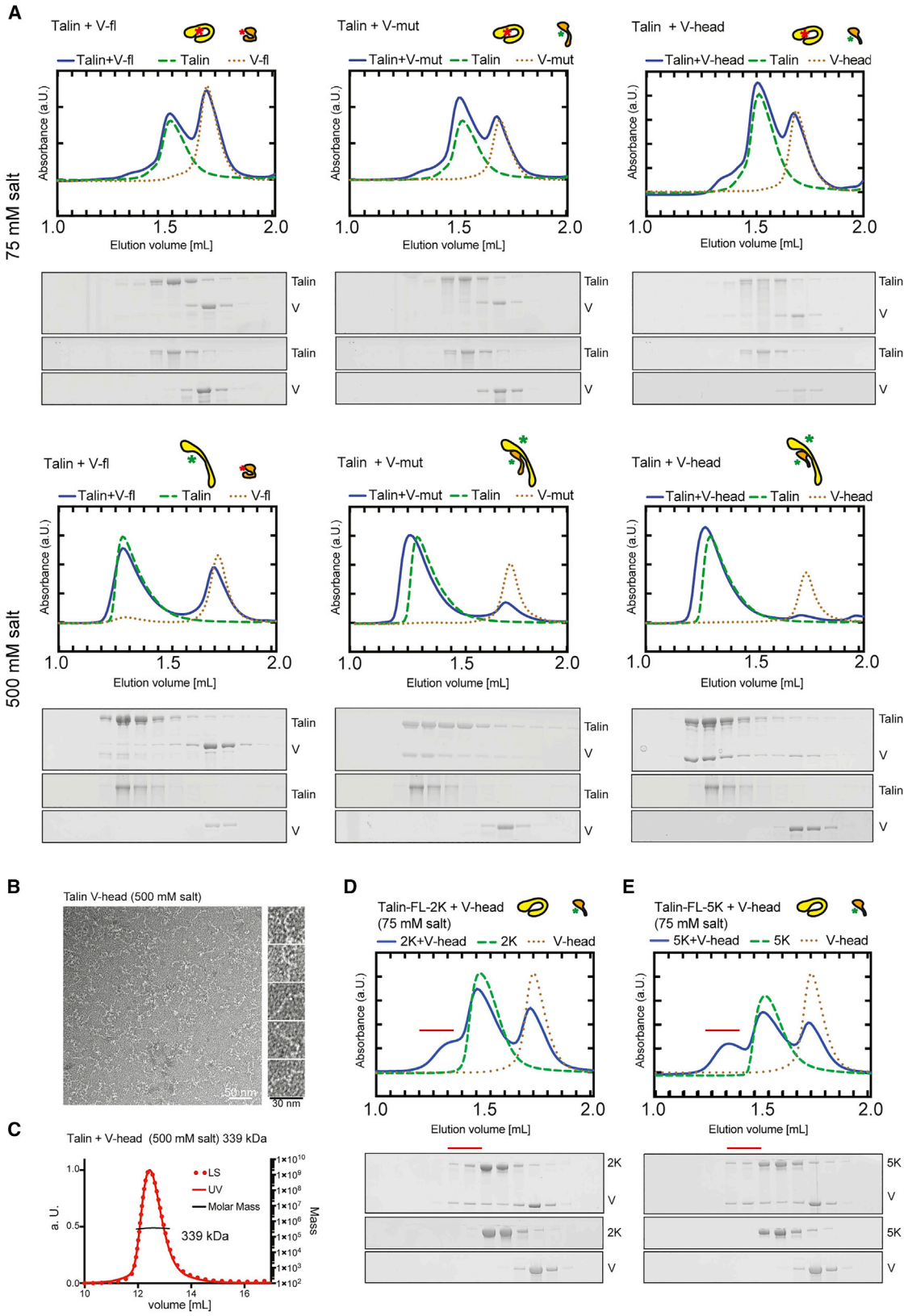

(legend on next page)

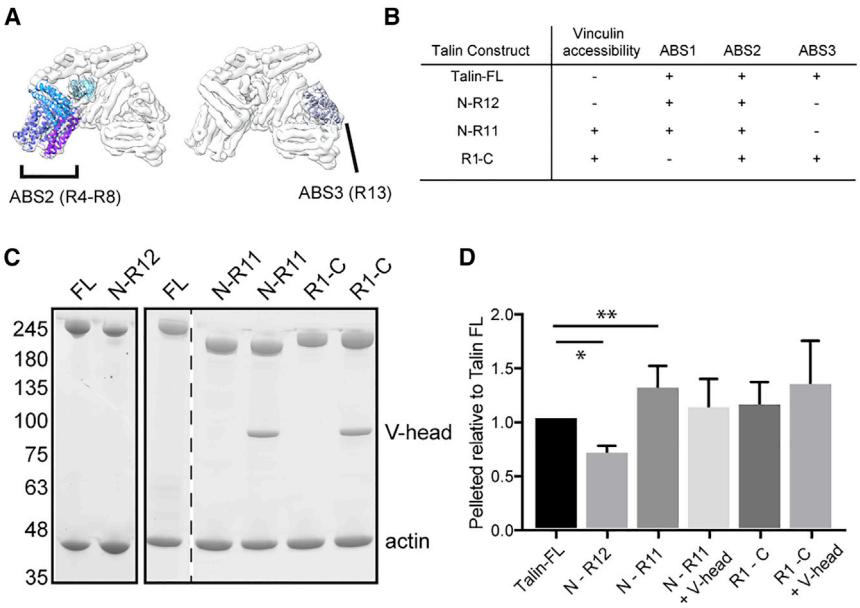

Talin Construct	Vinculin accessibility	ABS1	ABS2	ABS3
Talin-FL	-	+	+	+
N-R12	-	+	+	-
N-R11	+	+	+	-
R1-C	+	-	+	+

Figure 6. Talin-F-Actin Binding Assay

(A) Scheme of actin-binding domains ABS2 and ABS3 in the context of the autoinhibited talin structure.

(B) Table summarizing tested constructs for F-actin binding and vinculin accessibility of talin in compact conformation (75 mM KCl).

(C) Representative SDS-PAGE analysis of the F-actin co-sedimentation assay with various talin constructs at 75 mM salt. The dotted line indicates the elimination of an irrelevant lane from the gel.

(D) Quantification of the co-sedimented talin fragments. Data are represented as mean ± SD. N-R12, 0.68 ± 0.08; N-R11, 1.3 ± 0.2; N-R11 + V-head, 1.1 ± 0.3; R1-C, 1.1 ± 0.2; and R1-C + V-head, 1.3 ± 0.4. Differences between talin-FL and N-R12 as well as N-R11 are statistically significant (marked with *).

See also Figure S7.

the talin-vinculin complex likely corresponds to vinculin binding to R3. However, when we attempted to re-close talin in complex with the V-mut including the vinculin tail, vinculin was induced to be displaced from the complex (Figure S7A). This observation suggests that the vinculin tail competes with the talin R3 domain for binding to the vinculin head.

F-Actin Binding Is Enhanced by the Opening of Talin

Another major binding partner of talin is F-actin, which is located in the fourth layer of the FA. Acting as tension-generating machinery, actomyosin is thought to ensure the opening of talin by binding to two sites located at R4–R8 (ABS2) and R13 (ABS3; Figure 6A). Cell-based experiments with talin rod mutations suggested that ABS3 plays a role in recruiting talin to actin at the FA to activate talin, while ABS2 is critical for the maturation or growth of the FA (Atherton et al., 2015). Combining our structural findings, we hypothesized that the opening of talin is correlated with the engagement of talin to actin and tested the binding of various truncated talin variants to F-actin by co-sedimentation assays.

First, the truncated construct N-R12 was tested for binding to F-actin. In the tested condition at 75 mM KCl, N-R12, like talin-FL, employed an autoinhibited compact form (Figure 3F) that did not form a complex with vinculin (Figures 6B and S7H). Reflecting the fact that N-R12 lacks ABS3, the binding of F-actin to N-R12 was reduced compared to talin-FL (Figures 6C and 6D). Next, we tested the C-terminal truncation construct N-R11, which lacks the R12 domain. Without R12, talin N-R11 compaction is weak enough for vinculin to associate (Figures 6B and S7I). In contrast to N-R12, N-R11 bound F-actin with even higher amounts than talin-FL (Figures 6C and 6D), despite the fact that it lacks ABS3. Those results indicate that loosening the autoinhibitory lid (R12) of talin directly correlates with the activation of the F-actin binding of ABS2 as well as with vinculin binding. We also tested the truncation of the N-terminal FERM domain (R1-C) in the same way. R1-C showed binding similar to that of N-R11, although the described F-actin-binding activity of ABS1 at the FERM domain was missing from the fragment. R1-C was also capable of binding to the vinculin head (Figures 6B and S7J); however, it displayed no significant enhancement of F-actin binding.

Figure 5. Interaction Assays of Talin-FL and Vinculin under Various Conditions

(A) Talin-FL and vinculin reconstitution assays using size-exclusion chromatography (SEC). An ionic strength of 75 mM was used for the reconstitution assays shown in the upper panel and 500 mM in the lower panel. SDS-PAGE profiles (talin-vinculin mixture, talin control, vinculin control) of the peaks are shown below the SEC profiles. In order to achieve complex formation, it is necessary that both talin and vinculin employ open conformations (bottom-center and bottom-right). V-fl, vinculin full-length; V-mut, vinculin (N773A/E775A) mutant; V-head, vinculin head. Minor shoulders at the left side of talin peaks correspond to degraded talin without FERM domain. The control runs for talin come from the same experiment and the corresponding profile and SDS-PAGE are shown multiple times for comparison. The y-scaling has been adjusted for the different amplitudes of the chromatograms.

(B) Negative-stain EM image of vinculin head bound to open talin at 500 mM KCl.

(C) SEC-multi-angle light-scattering profile of V-head bound to open talin with a calculated molecular weight of 339 kDa, indicating that the complex is made with 1:1 stoichiometry. LS, light scattering, normalized; UV, absorbance.

(D) SEC reconstitution assay of talin-FL-2K mutant and vinculin head at 75 mM salt.

(E) SEC reconstitution assay of talin-FL-5K and vinculin head. The purified proteins have never been exposed to 500 mM salt, which facilitates the opening of talin. The complex formation of these mutants and V-head is observed (indicated by red lines). The control runs for V-head in (D) and (E) come from the same experiment and the corresponding profile and SDS-PAGE are shown twice for comparison.

See also Figures S6 and S7.

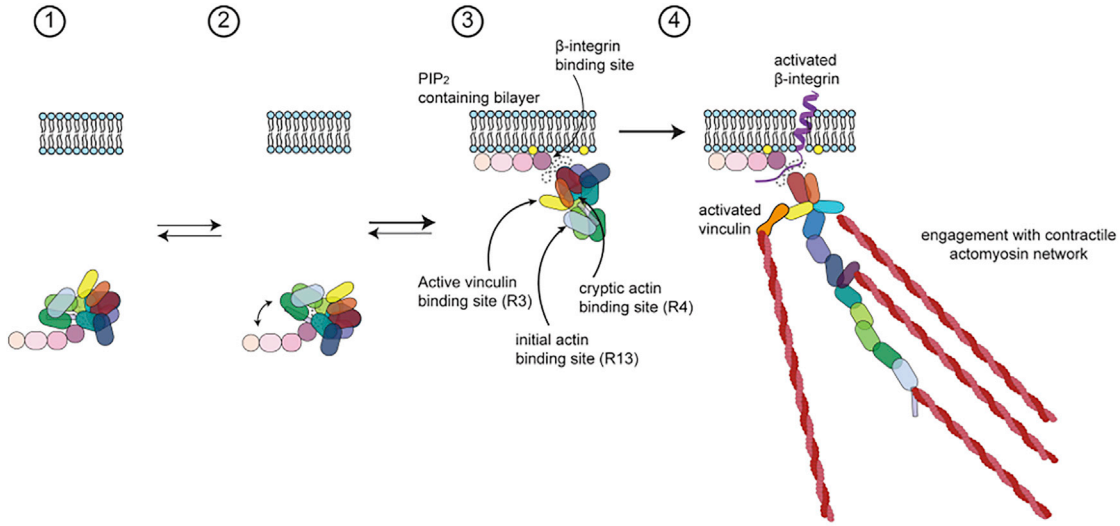

Figure 7. Model of Talin Activation

(1) Our structure of talin in the closed form reveals how inactivation is achieved through occlusion of functional sites. Rap1-mediated recruitment of talin to membranes can occur without breaking the closed formation of talin as the F0 and F1 subdomains are accessible.

(2) Our structural analysis also indicated that the closed form of talin is in equilibrium with a semi-opened state due to the instable FERM-lid connection (see Figure S1).

(3) Upon binding to the PIP_2-embedded membrane surface, the R12-F2 and R9-F3 interfaces are broken because of competitive interactions with PIP_2 and integrin, respectively (shown in Figure 1). The binding to the integrin tail hinders the F3-rod interaction (Wegener et al., 2007) and releases the rod domains from the FERM head as well as from the plasma membrane.

(4) The further opening of the rod domains may require the mechanical aid of actomyosin pulling via the ABS3 and ABS2 actin-binding sites. Vinculin may also take an active role in reinforcing the binding of talin to actin (Humphries et al., 2007).

DISCUSSION

Mechanism of Talin Regulation

In cellular environments, the concentration of talin can be as high as 50 μM (Zeiler et al., 2014; Zhu et al., 2017), making talin one of the most abundant components in cells. The activation of talin within FAs is essential; however, it is also critical that the adhesion components can be properly switched off to control cell attachment and migration. Therefore, the autoinhibited state of talin is essential (Ellis et al., 2013). Information is available about interactions among individual talin fragments (Goult et al., 2013; Song et al., 2012); however, the molecular architecture and the mechanism of talin's autoinhibition have been unknown in the regulatory context of full-length talin. We uncovered how talin can be folded to ensure its autoinhibition. A network of polar interactions keeps the 13 rod domains tangled into a compact globular architecture with the R4 domain buried in the core, thus shielding R4 and the actin-binding site ABS2 against actin binding. The compact architecture was further locked down by contacts between the F2 and F3 subdomains of the FERM head and the R12 and R9 rod domains, respectively. The PIP_2 binding FERM domain was masked by the R12 domain inhibiting the interaction of talin to the inner leaflet of the plasma membrane. The densities of R11–R13 are not well defined and show flexibility in the 3D classification (Figure S1C). This suggests that the connection between R12 and FERM domain F2 is loose. The interruption of this interaction may be sufficient to grant access to binding partners such as vinculin, whose binding cannot open the molecule completely. The conformational change of talin can be seen as an ensemble of open and closed states, which can be reversibly shifted by the change of salt concentration *in vitro*. The open conformation of talin likely mimics the activated talin stabilized by the actomyosin machinery during FA initiation.

Talin-Vinculin Complex Formation during Autoinhibition

We observed that one vinculin-binding site is readily available when full-length talin is released from the autoinhibited state without the application of any active force. Intriguingly, talin is able to reverse back to the closed conformation while vinculin-head is still bound to R3, but only in the absence of the vinculin tail. We speculate that this may hint at a mechanism to release vinculin when talin is inactivated and no longer engaged in the FA assembly. The closure of talin and concomitant folding of R3 may weaken the interaction of vinculin head to R3. In turn, the competition of vinculin tail for the head domain becomes more effective, resulting in the inactivation of vinculin and release from the complex in the autoinhibited form. It will be interesting to structurally map the interaction surface and find out which of the talin-binding partners can bind to the autoinhibited form of talin. Such an analysis will shed light on the functional role of talin in the cytosol and help to determine if there are preformed complexes that act as precursors of FA-related complexes. Along the same line, it is possible that talin dimerization might also occur upon talin activation and elongation. Binding to actin further expands the footprint of talin and exposes the C-terminal dimerization domain, as suggested previously (Goldmann et al., 1994), while dimerization appears

dispensable when talin is autoinhibited. Talin dimerization offers an additional layer of regulation and the possibility for larger complexes to be assembled from preformed FA subcomplexes. Further structural analysis of full-length talin in its active, elongated form in comparison with its autoinhibited form will provide a comprehensive view of talin function during FA initiation and maturation.

The Topological Positioning of Talin Is a Key Step in FA Activation

Our talin structure showed that the globular rod domains occlude the membrane-binding plane of the FERM domain. On the other hand, the N-terminal FERM F0-F1 subdomains and the C-terminal DD domain were not involved in maintaining the structural organization of the autoinhibited form of talin, indicating that those domains are freely accessible and not inhibited when talin is closed. In particular, F0 has been shown to be a key binding domain for Rap1, which has been suggested as the first step in the recruitment of talin to the cell-membrane surface (Zhu et al., 2017).

In addition, talin has a 30 amino-acid flexible linker between the F1 and F2 subdomains that separates F0-F1 from the globular autoinhibited structure (F2-DD). This separation may allow F0-F1 to ''search'' for cofactors. Our findings, together with previous results, suggest a model of how talin is recruited and correctly positioned at the membrane surface (Figure 7, model). Autoinhibited talin is recruited to the membrane via its freely accessible F0 subdomain in a Rap1-assisted manner. Thus, the FERM domain orchestrates the binding of Rap1 on the one hand (Zhu et al., 2017), while on the other it accesses the exposed, negatively charged plasma membrane via the flexible loop inserted in the F1 subdomain (Goult et al., 2010). This recruitment process increases the local concentration of PIP_2, due to the recruitment of PIPK1γ90 by the F3 subdomain (Di Paolo et al., 2002; Ling et al., 2002). PIP_2 may bind to talin, opening the R12 lid, thus shifting the conformational ensemble toward open structures. The F3-R9 interaction may then be abrogated (Figure 7, step 3), allowing the integrin tail to interact with F3.

This rearrangement releases the rod domains from the head domain (Figure 7, step 3), activating the interaction sites for various talin-binding proteins. The rod domains themselves can be readily approached by vinculin and actin (as shown in Figure 6), which could lead to the initiation of FA formation (Figure 7, step 4). Our actin co-sedimentation assays with truncated talin revealed that ABS2 is inhibited while talin is closed. This shows that the initial pulling of talin ABS3 by the actomyosin machinery aids the opening of talin to enable the accessibility of ABS2 as well as vinculin, as also shown in a previous report (Atherton et al., 2015). Finally, actin binding would enable actin retrograde force to exert tensile force on talin, enabling mechanical force to further stabilize talin opening (Sun et al., 2019). Our structure provides a mechanistic basis to understand the inhibition and activation of talin. Although our model is coherent, further testing is needed to validate key events. Furthermore, other yet-unknown activating factors may be involved to tightly regulate the inhibition and activation of talin or to modulate individual functions of talin.

STAR★METHODS

Detailed methods are provided in the online version of this paper and include the following:

- KEY RESOURCES TABLE
- LEAD CONTACT AND MATERIALS AVAILABILITY
- EXPERIMENTAL MODEL AND SUBJECT DETAILS
- METHOD DETAILS
  - Protein purification
  - Gradient Fixation (GraFix) of talin samples
  - Mass spectrometry
  - Negative-stain electron microscopy
  - Cryo-EM analysis of full-length talin
  - Molecular dynamics for flexible fitting
  - Estimation of interaction energies
  - F-Actin co-sedimentation assay
  - Analytical size-exclusion chromatography
  - Dynamic Light-Scattering (DLS)
  - Size-Exclusion Chromatography Coupled with Multi-Angle Light-Scattering (SEC-MALS)
- QUANTIFICATION AND STATISTICAL ANALYSIS
- DATA AND CODE AVAILABILITY

SUPPLEMENTAL INFORMATION

Supplemental Information can be found online at https://doi.org/10.1016/j.cell.2019.08.034.

ACKNOWLEDGEMENTS

We thank Carsten Grashoff and Giovanni Cardone for assistance at various stages of the project, Elena Conti, Wolfgang Baumeister, and the biochemistry- and cryo-EM core facilities for resources and infrastructure (Max Planck Institute of Biochemistry). N.M. acknowledges the Max Planck Society, Germany, Boehringer Ingelheim Foundation Plus 3 Program, Germany, and the European Research Council (ERC-CoG, 724209), European Union, for funding. N.M. is a recipient of the EMBO Young Investigator award. C.F.K. is supported by an EMBO long-term fellowship (EMBO ALTF 450-2017) and an Alexander von Humboldt (Germany) research fellowship for postdoctoral researchers.

AUTHOR CONTRIBUTIONS

Conceptualization, N.M.; Methodology, D.D., M.Z., C.B., and N.M.; Investigation, D.D., S.S., C.F.K., M.Z., and C.B.; Writing, N.M. and D.D.; Resources, N.M. and R.F.; Funding Acquisition, N.M.; Supervision, N.M.

DECLARATION OF INTERESTS

The authors declare no competing interests.

Received: January 2, 2019
Revised: April 4, 2019
Accepted: August 16, 2019
Published: September 19, 2019

REFERENCES

Afonine, P.V., Poon, B.K., Read, R.J., Sobolev, O.V., Terwilliger, T.C., Urzhumtsev, A., and Adams, P.D. (2018). Real-space refinement in PHENIX for cryo-EM and crystallography. Acta Crystallogr. D Struct. Biol. *74*, 531–544.

Anthis, N.J., Wegener, K.L., Ye, F., Kim, C., Goult, B.T., Lowe, E.D., Vakonakis, I., Bate, N., Critchley, D.R., Ginsberg, M.H., et al. (2009). The structure of an

integrin/talin complex reveals the basis of inside-out signal transduction. EMBO J. *28*, 3623–3632.

Atherton, P., Stutchbury, B., Wang, D.-Y., Jethwa, D., Tsang, R., Meiler-Rodriguez, E., Wang, P., Bate, N., Zent, R., Barsukov, I.L., et al. (2015). Vinculin controls talin engagement with the actomyosin machinery. Nat. Commun. *6*, 10038.

Austen, K., Ringer, P., Mehlich, A., Chrostek-Grashoff, A., Kluger, C., Klingner, C., Sabass, B., Zent, R., Rief, M., and Grashoff, C. (2015). Extracellular rigidity sensing by talin isoform-specific mechanical linkages. Nat. Cell Biol. *17*, 1597–1606.

Bachir, A.I., Zareno, J., Moissoglu, K., Plow, E.F., Gratton, E., and Horwitz, A.R. (2014). Integrin-associated complexes form hierarchically with variable stoichiometry in nascent adhesions. Curr. Biol. *24*, 1845–1853.

Bai, X.-C., Rajendra, E., Yang, G., Shi, Y., and Scheres, S.H.W. (2015). Sampling the conformational space of the catalytic subunit of human γ-secretase. eLife *4*, e11182.

Borgon, R.A., Vonrhein, C., Bricogne, G., Bois, P.R.J., and Izard, T. (2004). Crystal structure of human vinculin. Structure *12*, 1189–1197.

Calderwood, D.A., Campbell, I.D., and Critchley, D.R. (2013). Talins and kindlins: partners in integrin-mediated adhesion. Nat. Rev. Mol. Cell Biol. *14*, 503–517.

Carisey, A., Tsang, R., Greiner, A.M., Nijenhuis, N., Heath, N., Nazgiewicz, A., Kemkemer, R., Derby, B., Spatz, J., and Ballestrem, C. (2013). Vinculin regulates the recruitment and release of core focal adhesion proteins in a force-dependent manner. Curr. Biol. *23*, 271–281.

Case, L.B., Baird, M.A., Shtengel, G., Campbell, S.L., Hess, H.F., Davidson, M.W., and Waterman, C.M. (2015). Molecular mechanism of vinculin activation and nanoscale spatial organization in focal adhesions. Nat. Cell Biol. *17*, 880–892.

Chacón, P., and Wriggers, W. (2002). Multi-resolution contour-based fitting of macromolecular structures. J. Mol. Biol. *317*, 375–384.

Chinthalapudi, K., Rangarajan, E.S., and Izard, T. (2018). The interaction of talin with the cell membrane is essential for integrin activation and focal adhesion formation. Proc. Natl. Acad. Sci. USA *115*, 10339–10344.

Cohen, D.M., Chen, H., Johnson, R.P., Choudhury, B., and Craig, S.W. (2005). Two distinct head-tail interfaces cooperate to suppress activation of vinculin by talin. J. Biol. Chem. *280*, 17109–17117.

Cox, J., and Mann, M. (2008). MaxQuant enables high peptide identification rates, individualized p.p.b.-range mass accuracies and proteome-wide protein quantification. Nat. Biotechnol. *26*, 1367–1372.

Desiniotis, A., and Kyprianou, N. (2011). Significance of talin in cancer progression and metastasis. Int. Rev. Cell Mol. Biol. *289*, 117–147.

Di Paolo, G., Pellegrini, L., Letinic, K., Cestra, G., Zoncu, R., Voronov, S., Chang, S., Guo, J., Wenk, M.R., and De Camilli, P. (2002). Recruitment and regulation of phosphatidylinositol phosphate kinase type 1 gamma by the FERM domain of talin. Nature *420*, 85–89.

Elliott, P.R., Goult, B.T., Kopp, P.M., Bate, N., Grossmann, J.G., Roberts, G.C.K., Critchley, D.R., and Barsukov, I.L. (2010). The Structure of the talin head reveals a novel extended conformation of the FERM domain. Structure *18*, 1289–1299.

Ellis, S.J., Goult, B.T., Fairchild, M.J., Harris, N.J., Long, J., Lobo, P., Czerniecki, S., Van Petegem, F., Schöck, F., Peifer, M., et al. (2013). Talin autoinhibition is required for morphogenesis. Curr. Biol. *23*, 1825–1833.

Emsley, P., Lohkamp, B., Scott, W.G., and Cowtan, K. (2010). Features and development of Coot. Acta Crystallogr. D Biol. Crystallogr. *66*, 486–501.

Fang, K.-P., Dai, W., Ren, Y.-H., Xu, Y.-C., Zhang, S.-M., and Qian, Y.-B. (2016). Both Talin-1 and Talin-2 correlate with malignancy potential of the human hepatocellular carcinoma MHCC-97 L cell. BMC Cancer *16*, 45.

Fillingham, I., Gingras, A.R., Papagrigoriou, E., Patel, B., Emsley, J., Critchley, D.R., Roberts, G.C.K., and Barsukov, I.L. (2005). A vinculin binding domain from the talin rod unfolds to form a complex with the vinculin head. Structure *13*, 65–74.

Garcia-Alvarez, B., de Pereda, J.M., Calderwood, D.A., Ulmer, T.S., Critchley, D., Campbell, I.D., Ginsberg, M.H., and Liddington, R.C. (2003). Structural determinants of integrin recognition by talin. Mol. Cell *11*, 49–58.

Geiger, B., Spatz, J.P., and Bershadsky, A.D. (2009). Environmental sensing through focal adhesions. Nat. Rev. Mol. Cell Biol. *10*, 21–33.

Gingras, A.R., Ziegler, W.H., Frank, R., Barsukov, I.L., Roberts, G.C.K., Critchley, D.R., and Emsley, J. (2005). Mapping and consensus sequence identification for multiple vinculin binding sites within the talin rod. J. Biol. Chem. *280*, 37217–37224.

Gingras, A.R., Bate, N., Goult, B.T., Hazelwood, L., Canestrelli, I., Grossmann, J.G., Liu, H., Putz, N.S.M., Roberts, G.C.K., Volkmann, N., et al. (2008). The structure of the C-terminal actin-binding domain of talin. EMBO J. *27*, 458–469.

Goldmann, W.H., Bremer, A., Häner, M., Aebi, U., and Isenberg, G. (1994). Native talin is a dumbbell-shaped homodimer when it interacts with actin. J. Struct. Biol. *112*, 3–10.

Goult, B.T., Bouaouina, M., Elliott, P.R., Bate, N., Patel, B., Gingras, A.R., Grossmann, J.G., Roberts, G.C.K., Calderwood, D.A., Critchley, D.R., et al. (2010). Structure of a double ubiquitin-like domain in the talin head: a role in integrin activation. EMBO J. *29*, 1069–1080.

Goult, B.T., Xu, X.-P., Gingras, A.R., Swift, M., Patel, B., Bate, N., Kopp, P.M., Barsukov, I.L., Critchley, D.R., Volkmann, N., et al. (2013). Structural studies on full-length talin1 reveal a compact auto-inhibited dimer: implications for talin activation. J. Struct. Biol. *184*, 21–32.

Goult, B.T., Yan, J., and Schwartz, M.A. (2018). Talin as a mechanosensitive signaling hub. J. Cell Biol. *217*, 3776–3784.

Haining, A.W.M., Lieberthal, T.J., and Del Río Hernández, A. (2016). Talin: a mechanosensitive molecule in health and disease. FASEB J. *30*, 2073–2085.

Harburger, D.S., and Calderwood, D.A. (2009). Integrin signalling at a glance. J. Cell Sci. *122*, 159–163.

Hemmings, L., Rees, D.J., Ohanian, V., Bolton, S.J., Gilmore, A.P., Patel, B., Priddle, H., Trevithick, J.E., Hynes, R.O., and Critchley, D.R. (1996). Talin contains three actin-binding sites each of which is adjacent to a vinculin-binding site. J. Cell Sci. *109*, 2715–2726.

Heymann, J.B., and Belnap, D.M. (2007). Bsoft: image processing and molecular modeling for electron microscopy. J. Struct. Biol. *157*, 3–18.

Humphries, J.D., Wang, P., Streuli, C., Geiger, B., Humphries, M.J., and Ballestrem, C. (2007). Vinculin controls focal adhesion formation by direct interactions with talin and actin. J. Cell Biol. *179*, 1043–1057.

Izard, T., Evans, G., Borgon, R.A., Rush, C.L., Bricogne, G., and Bois, P.R.J. (2004). Vinculin activation by talin through helical bundle conversion. Nature *427*, 171–175.

Johnson, R.P., and Craig, S.W. (1994). An intramolecular association between the head and tail domains of vinculin modulates talin binding. J. Biol. Chem. *269*, 12611–12619.

Kanchanawong, P., Shtengel, G., Pasapera, A.M., Ramko, E.B., Davidson, M.W., Hess, H.F., and Waterman, C.M. (2010). Nanoscale architecture of integrin-based cell adhesions. Nature *468*, 580–584.

Kumar, A., Ouyang, M., Van den Dries, K., McGhee, E.J., Tanaka, K., Anderson, M.D., Groisman, A., Goult, B.T., Anderson, K.I., and Schwartz, M.A. (2016). Talin tension sensor reveals novel features of focal adhesion force transmission and mechanosensitivity. J. Cell Biol. *213*, 371–383.

Legate, K.R., Wickström, S.A., and Fässler, R. (2009). Genetic and cell biological analysis of integrin outside-in signaling. Genes Dev. *23*, 397–418.

Ling, K., Doughman, R.L., Firestone, A.J., Bunce, M.W., and Anderson, R.A. (2002). Type I gamma phosphatidylinositol phosphate kinase targets and regulates focal adhesions. Nature *420*, 89–93.

Liu, J., Wang, Y., Goh, W.I., Goh, H., Baird, M.A., Ruehland, S., Teo, S., Bate, N., Critchley, D.R., Davidson, M.W., et al. (2015). Talin determines the nanoscale architecture of focal adhesions. Proc. Natl. Acad. Sci. USA *112*, E4864–E4873.

Maier, J.A., Martinez, C., Kasavajhala, K., Wickstrom, L., Hauser, K.E., and Simmerling, C. (2015). ff14SB: Improving the Accuracy of Protein Side Chain and Backbone Parameters from ff99SB. J. Chem. Theory Comput. *11*, 3696–3713.

Margadant, F., Chew, L.L., Hu, X., Yu, H., Bate, N., Zhang, X., and Sheetz, M. (2011). Mechanotransduction in vivo by repeated talin stretch-relaxation events depends upon vinculin. PLoS Biol. *9*, e1001223.

Mastronarde, D.N. (2005). Automated electron microscope tomography using robust prediction of specimen movements. J. Struct Biol. *152*, 36–51.

Molony, L., McCaslin, D., Abernethy, J., Paschal, B., and Burridge, K. (1987). Properties of talin from chicken gizzard smooth muscle. J. Biol. Chem. *262*, 7790–7795.

Nieswandt, B., Moser, M., Pleines, I., Varga-Szabo, D., Monkley, S., Critchley, D., and Fässler, R. (2007). Loss of talin1 in platelets abrogates integrin activation, platelet aggregation, and thrombus formation in vitro and in vivo. J. Exp. Med. *204*, 3113–3118.

Onufriev, A., Bashford, D., and Case, D.A. (2000). Modification of the generalized Born model suitable for macromolecules. J. Phys. Chem. B *104*, 3712–3720.

Orłowski, A., Kukkurainen, S., Pöyry, A., Rissanen, S., Vattulainen, I., Hytönen, V.P., and Róg, T. (2015). PIP_2 and Talin Join Forces to Activate Integrin. J. Phys. Chem. B *119*, 12381–12389.

Papagrigoriou, E., Gingras, A.R., Barsukov, I.L., Bate, N., Fillingham, I.J., Patel, B., Frank, R., Ziegler, W.H., Roberts, G.C.K., Critchley, D.R., et al. (2004). Activation of a vinculin-binding site in the talin rod involves rearrangement of a five-helix bundle. EMBO J. *23*, 2942–2951.

Parsons, J.T., Horwitz, A.R., and Schwartz, M.A. (2010). Cell adhesion: integrating cytoskeletal dynamics and cellular tension. Nat. Rev. Mol. Cell Biol. *11*, 633–643.

Pettersen, E.F., Goddard, T.D., Huang, C.C., Couch, G.S., Greenblatt, D.M., Meng, E.C., and Ferrin, T.E. (2004). UCSF Chimera--a visualization system for exploratory research and analysis. J. Comput. Chem. *25*, 1605–1612.

Plak, K., Pots, H., Van Haastert, P.J.M., and Kortholt, A. (2016). Direct Interaction between TalinB and Rap1 is necessary for adhesion of Dictyostelium cells. BMC Cell Biol. *17*, 1.

Punjani, A., Rubinstein, J.L., Fleet, D.J., and Brubaker, M.A. (2017). cryoSPARC: algorithms for rapid unsupervised cryo-EM structure determination. Nat. Methods *14*, 290–296.

Rees, D.J., Ades, S.E., Singer, S.J., and Hynes, R.O. (1990). Sequence and domain structure of talin. Nature *347*, 685–689.

Salomon-Ferrer, R., Case, D.A., and Walker, R.C. (2013). An overview of the Amber biomolecular simulation package. Wiley Interdiscip. Rev. Comput. Mol. Sci. *3*, 198–210.

Schindelin, J., Arganda-Carreras, I., Frise, E., Kaynig, V., Longair, M., Pietzsch, T., Preibisch, S., Rueden, C., Saalfeld, S., Schmid, B., et al. (2012). Fiji: an open-source platform for biological-image analysis. Nat. Methods *9*, 676–682.

Song, X., Yang, J., Hirbawi, J., Ye, S., Perera, H.D., Goksoy, E., Dwivedi, P., Plow, E.F., Zhang, R., and Qin, J. (2012). A novel membrane-dependent on/off switch mechanism of talin FERM domain at sites of cell adhesion. Cell Res. *22*, 1533–1545.

Stark, H. (2010). GraFix: stabilization of fragile macromolecular complexes for single particle cryo-EM. Methods Enzymol. *481*, 109–126.

Sun, Z., Costell, M., and Fässler, R. (2019). Integrin activation by talin, kindlin and mechanical forces. Nat. Cell Biol. *21*, 25–31.

Tadokoro, S., Shattil, S.J., Eto, K., Tai, V., Liddington, R.C., de Pereda, J.M., Ginsberg, M.H., and Calderwood, D.A. (2003). Talin binding to integrin beta tails: a final common step in integrin activation. Science *302*, 103–106.

Tanentzapf, G., and Brown, N.H. (2006). An interaction between integrin and the talin FERM domain mediates integrin activation but not linkage to the cytoskeleton. Nat. Cell Biol. *8*, 601–606.

Wegener, K.L., Partridge, A.W., Han, J., Pickford, A.R., Liddington, R.C., Ginsberg, M.H., and Campbell, I.D. (2007). Structural basis of integrin activation by talin. Cell *128*, 171–182.

Wegener, K.L., Basran, J., Bagshaw, C.R., Campbell, I.D., Roberts, G.C.K., Critchley, D.R., and Barsukov, I.L. (2008). Structural basis for the interaction between the cytoplasmic domain of the hyaluronate receptor layilin and the talin F3 subdomain. J. Mol. Biol. *382*, 112–126.

Winkler, J., Lünsdorf, H., and Jockusch, B.M. (1997). Energy-filtered electron microscopy reveals that talin is a highly flexible protein composed of a series of globular domains. Eur. J. Biochem. *243*, 430–436.

Yang, J., Zhu, L., Zhang, H., Hirbawi, J., Fukuda, K., Dwivedi, P., Liu, J., Byzova, T., Plow, E.F., Wu, J., et al. (2014). Conformational activation of talin by RIAM triggers integrin-mediated cell adhesion. Nat. Commun. *5*, 5880.

Yao, M., Goult, B.T., Chen, H., Cong, P., Sheetz, M.P., and Yan, J. (2014). Mechanical activation of vinculin binding to talin locks talin in an unfolded conformation. Sci. Rep. *4*, 4610.

Zaidel-Bar, R., Ballestrem, C., Kam, Z., and Geiger, B. (2003). Early molecular events in the assembly of matrix adhesions at the leading edge of migrating cells. J. Cell Sci. *116*, 4605–4613.

Zeiler, M., Moser, M., and Mann, M. (2014). Copy number analysis of the murine platelet proteome spanning the complete abundance range. Mol. Cell. Proteomics *13*, 3435–3445.

Zhang, K. (2016). Gctf: Real-time CTF determination and correction. J. Struct. Biol. *193*, 1–12.

Zheng, S.Q., Palovcak, E., Armache, J.-P., Verba, K.A., Cheng, Y., and Agard, D.A. (2017). MotionCor2: anisotropic correction of beam-induced motion for improved cryo-electron microscopy. Nat. Methods *14*, 331–332.

Zhu, L., Yang, J., Bromberger, T., Holly, A., Lu, F., Liu, H., Sun, K., Klapproth, S., Hirbawi, J., Byzova, T.V., et al. (2017). Structure of Rap1b bound to talin reveals a pathway for triggering integrin activation. Nat. Commun. *8*, 1744.

Zivanov, J., Nakane, T., Forsberg, B.O., Kimanius, D., Hagen, W.J., Lindahl, E., and Scheres, S.H. (2018). New tools for automated high-resolution cryo-EM structure determination in RELION-3. eLife *7*, e42166.

STAR★METHODS

KEY RESOURCES TABLE

REAGENT or RESOURCE	SOURCE	IDENTIFIER
Bacterial and Virus Strains		
Escherichia coli, BL21-Gold (DE3)	Agilent	Cat# 230132
Escherichia coli, XL1-Blue	Agilent	Cat# 200249
Chemicals, Peptides, and Recombinant Proteins		
N-2-Hydroxyethylpiperazine-N'-2-ethanesulfonic acid (HEPES)	Roth	Cat# 9105.3
Potassium Chloride	Roth	Cat# 6781.1
Sodium Chloride	Merck	Cat# 1.06404
Ethylenediaminetetraacetic acid (EDTA)	VWR	Cat# 1.08418.0250
Dithiothreitol (DTT)	AppliChem	Cat# A1101
2-Mercaptoethanol	AppliChem	Cat# 4338.0100
D(+)-Saccharose	Roth	Cat# 4621.1
Glutharaldehyde	Sigma	Cat# 340855
Octyl β-D-glucopyranoside	Sigma	Cat# O8001-500MG
Uranyl acetate 2%	Science Services	Cat# E22400-2
Tris(hydroxymethyl)aminomethane (Tris/Trizma Base)	Sigma	Cat# T1503
4-Morpholineethanesulfonic acid (MES)	Sigma	Cat# M8250-250G
Imidazol	Merck	Cat# 1.04716.1000
Actin (rabbit skeletal muscle alpha actin)	Hypermol	Cat# 8101-03
L-Glutathione (reduced)	VWR	Cat# 0399-50G
Glyercol 99.5%	Roth	Cat# 3783.1
cOmplete EDTA-free, 3 x 20 Tablets	Roche	Cat# 5056489001
Magnesium chloride	Roth	Cat# 2189.2
Calcium chloride	Roth	Cat# 5239.2
Adenosine 5'-triphosphate disodium salt hydrate	Sigma	Cat# A2383-10G
Protein Marker VI (10 - 245) pre-stained	AppliChem	Cat# A8889.0500
Critical Commercial Assays		
NucleoSpin Plasmid EasyPure	Macherey Nagel	Cat# 740727.250
Roche cOmplete His-Tag purification column	Roche Diagnostics	Cat# 06781535001
HiTrap Q HP column	GE Healthcare	Cat# 17-1154-01
16/600 Superdex 200 GL	GE Healthcare	Cat# 28-9893-35
3.2/300 Superdex 200 increase	GE Healthcare	Cat# 28-9909-46
3.2/300 Superose 6 increase	GE Healthcare	Cat# 29-0915-98
GSTrap FF, HiTrap GSH/GST	GE Healthcare	Cat# 17-5131-01
Deposited Data		
Cryo-EM map of talin-FL	This study	EMD-4772
Atomic model of talin-FL	This study	PDB 6R9T
Experimental Models: Organisms/Strains		
Escherichia coli, BL21-Gold (DE3)	Agilent	Cat# 230132
Escherichia coli, XL1-Blue	Agilent	Cat# 200249
Oligonucleotides		
DNA Primers, see Table S2	This study	N/A
Recombinant DNA		
Plasmid DNAs, see Table S2	This study	N/A

(*Continued on next page*)

Continued

REAGENT or RESOURCE	SOURCE	IDENTIFIER
Software and Algorithms		
Serial EM	Mastronarde, 2005	http://bio3d.colorado.edu/SerialEM
Gctf	Zhang, 2016	https://en.wikibooks.org/w/index.php?title=Software_Tools_For_Molecular_Microscopy&stable=0#Gctf
Gautomatch	Andrew Carter lab, unpublished	https://www.mrc-lmb.cam.ac.uk/kzhang/
MotionCor2	Zheng et al., 2017	https://msg.ucsf.edu/software
RELION	Zivanov et al., 2018	http://www3.mrc-lmb.cam.ac.uk/relion
cryoSPARC	Punjani et al., 2017	https://cryosparc.com/
UCSF Chimera	Pettersen et al., 2004	http://www.cgl.ucsf.edu/chimera/
Bsoft	Heymann and Belnap, 2007	https://lsbr.niams.nih.gov/bsoft/
Coot	Emsley et al., 2010	http://www2.mrc-lmb.cam.ac.uk/Personal/pemsley/coot/
PHENIX	Afonine et al. 2018	https://www.phenix-online.org/
UNICORN	GE Healthcare	https://www.gelifesciences.com
OmniSEC	Malvern	https://www.malvernpanalytical.com
PRISM	Graphpad	https://www.graphpad.com/scientific-software/prism/
Amber 16/18	Salomon-Ferrer et al., 2013	http://ambermd.org/AmberTools.php
MaxQuant	Cox and Mann, 2008	https://www.maxquant.org/maxquant/
Other		
Carbon-coated copper grids	Home-made	N/A
Quantifoil Cu 200 mesh R1.2/1.3 grids	QUANTIFOIL	N/A

LEAD CONTACT AND MATERIALS AVAILABILITY

Further information and requests for resources and reagents should be directed to and will be fulfilled by the Lead Contact, Naoko Mizuno (mizuno@biochem.mpg.de). Materials and plasmids generated in this study (see Table S2) are available upon request.

EXPERIMENTAL MODEL AND SUBJECT DETAILS

E. coli XL1-blue was cultured at 37°C in LB medium supplemented with 100 μg/ml ampicillin for plasmid DNA extraction. *E. coli* BL21(DE3) gold was cultured at 37°C in ZY auto-induction medium supplemented with 100 μg/ml ampicillin until reaching an OD_{600} >2. The temperature was then switched to 16°C for protein expression overnight. Plasmids used for protein production are listed in Table S2.

METHOD DETAILS

Protein purification

Expression constructs of full-length talin1 (talin-FL) were prepared using human talin1 DNA (a gift from Christophe Le Clainche). DNA of talin-FL was amplified using PCR and subcloned into a pCB homemade expression vector with a His tag at the C-terminus for bacterial or mammalian cells. Talin1 was expressed in *E. coli* BL21 (DE3) gold using ZY auto-induction medium. Cells were lysed by sonication in 50 mM Tris-HCl pH 7.8, 500 mM NaCl, 10 mM imidazole, 1 mM DTT, 5 mM EDTA, purified by nickel-affinity chromatography (complete His-Tag purification column, Roche) and anion exchange (HiTrap Q HP, GE Healthcare). The His-tag was removed using 3C protease and proteins were further purified by size-exclusion chromatography using a Superdex 200 16/600 column (GE Healthcare) in 20 mM HEPES pH 7.8, 75 mM KCl, 0.5 mM β-Mercaptoethanol and 0.5 mM EDTA and 10% glycerol.

Talin truncation and mutation variants were obtained using mouse talin FL (pLPCXmod-Talin1-Ypet; a gift from Carsten Grashoff) as a template and cloned into homemade expression vectors (pCB and pEC vectors). Mouse talin constructs used in this study were 1-2482 (talin -ΔDD), 482-2541 (R1-C) 1-2294 (N-R12), 1-2141 (N-R11), 482-1655 (R1-R8), 482-913 (R1-R3), 913-1655 (R4-R8), talin mutant E2288K/E2294K/D2297K/E2299K/D2300K (talin-FL-5K) as well as talin mutant E2288K/E2294K (talin-FL-2K) (see Table S2).

The DNA fragments were amplified using PCR and subcloned into a pCB vector containing a cleavable N-terminal Venus-His8-Sumo tag or His tag. Proteins were expressed in *E. coli* BL21 (DE3) gold in ZY auto-induction medium. Talin truncation variants were purified using the same procedure as talin-FL. Tags were removed using 3C or Senp2 protease and proteins were further purified by size-exclusion chromatography using a Superdex 200 16/600 column (GE Healthcare) with 20 mM HEPES pH 7.5, 75 mM NaCl, 0.5 mM EDTA and 0.5 mM β-Mercaptoethanol.

Vinculin constructs were designed based on a previous report (Cohen et al., 2005) and cloned into homemade pEC vectors containing N-terminal GST-His tag and a 3C-cleavage site. V-head contains a.a. 1-851. Proteins were purified using His-affinity purification methods and eluted with 500 mM imidazole. Protein fragments were cleaved with 3C protease and dialyzed over night against 20 mM HEPES at pH 7.8, 100 mM KCl, 0.5 mM β-Mercaptoethanol, concentrated and subsequently applied to size-exclusion chromatography (Superdex 200 16/600, GE Healthcare). All purified proteins were stored at −80°C. Analytical size-exclusion chromatography experiments using talin were performed in 20 mM HEPES at pH 7.8, 0.5 mM β-Mercaptoethanol, 0.5 mM EDTA either with 75 or 500 mM KCl to test the influence of salt on the conformational change observed under negative-stain EM.

Gradient Fixation (GraFix) of talin samples

To stabilize weak protein-protein interactions, the GraFix crosslinking protocol was used (Stark, 2010). Talin samples were subjected to a sucrose and glutaraldehyde gradient of 10-30% and 0-0.2%, respectively, in a buffer containing 20 mM HEPES (pH 7.5), 75 mM KCl, 0.5 mM β-Mercaptoethanol and 0.5 mM EDTA. Gradients were prepared in 2.2 ml ultracentrifuge tubes (open-top polyclear tubes, Seton) using a Gradient Station machine (model ip, Biocomp). 50 μl of talin samples at a concentration of 5 mg/ml (approximately 18.5 μM) were placed on top of the gradients and centrifuged in a TLS55 rotor (Beckman Coulter) at 50 000 rpm, for 6 h at 4°C, using an Optima Max-XP ultracentrifuge (Beckman Coulter). 100 μl-Fractions were collected manually from top to bottom and quenched with 100 mM Tris (pH 7.5). Fractions containing the monomeric or dimeric talin, as determined by SDS-PAGE were pooled, concentrated, and buffer-exchanged to 20 mM HEPES (pH 7.5), 75 mM KCl, 0.5 mM β-Mercaptoethanol and 0.5 mM EDTA to remove excess sucrose using Amicon Ultra centrifugal filters (0.5 ml, 50 MWCO).

Mass spectrometry

For validating the full-length coverage of the protein sequence, the talin-FL sample was subjected to peptide mass fingerprinting analysis. The sample was diluted in equal volume of buffer containing 2% sodium deoxycholate (SDC), 20 mM TCEP and 80 mM chloroacetamide in 25 mM Tris at pH 8.5 and incubated at 37°C for 20 min. The sample was then further diluted with LC-MS grade water to reduce the SDC concentration to less than 0.5% and directly digested with 1 μg of trypsin (Promega) overnight. The peptides were then acidified and purified via SDB-SCX StageTips and analysed in a Q Exactive HF mass spectrometer using a 75 min gradient. Raw data were processed using the MaxQuant platform and all identifications were filtered at 1% false discovery rate (FDR).

Negative-stain electron microscopy

For negative-stain EM, homemade carbon-coated grids were prepared and glow discharged before use. 5 μl of sample was applied and incubated for 1 min, blotted, washed twice in two drops of water and stained in 2% uranyl acetate for 1 min. The prepared specimens were visualized with a FEI CM200 with an operating voltage of 160 kV equipped with an Eagle CCD camera with a pixel size of 2.16 Å/pix or with a FEI Tecnai F20 at 200 kV with an Eagle CCD camera with a pixel size of 2.21 Å/pix. For 2D classifications, particles were manually or automatically picked using RELION (Zivanov et al., 2018) and extracted in 276 Å boxes. For shape assessment, 1102 (talin-ΔDD) and 5678 (talin-FL V-head complex, treated with GraFix method for stabilization) particles were selected for reference-free 2D classification using RELION, resulting in 2D class averages. The lengths of open talin were measured using bshow in BSOFT (Heymann and Belnap, 2007). Five images of negatively stained talin were filtered using median filter (n=6) as well as Gaussian filter (sigma=4) to enhance the contrast of the protein densities. Particles showing clear boundaries were manually selected and their contour length was measured using the 'filament' option in BSOFT, facilitating the tracing of elongated, string-like particles. The histogram was created from a population size of N = 89, and the distribution was fit to normal distribution (average 560 Å, S.D. 170 Å).

Cryo-EM analysis of full-length talin

Samples for cryo-EM were applied to glow-discharged R1.2/1.3 Cu 200 mesh holey carbon grids at a concentration of 0.3 mg/mL in 20 mM HEPES at pH 7.8, 75 mM KCl, 0.5 mM β-Mercaptoethanol, 0.5 mM EDTA to ensure the compact formation of talin based on the DLS experiment shown in Figure 3D. Under salt concentrations of 200 mM KCl and higher, the compact formation of talin molecule was compromised in the cryo-EM environment, yielding poor 2D averages (Figure S2D). The grids were blotted at ~95% humidity at 4°C for 4 s and plunged into liquid ethane-propane using a Vitrobot Mark IV (FEI). 11007 micrographs were collected on a Titan Krios (FEI) at 300 kV equipped with a K2 Summit direct electron detector and a quantum energy filter (20 e-V)(Gatan). Micrographs were exposed for 10 s at 7.68 e-/Å2/s (total dose 76.8 e-/Å2) and 40 frames were collected in counting mode (pixel size 1.06 Å/pixel). Defocus was varied between -1 and -3 μm in steps of 0.3 μm. Movies were aligned, gain-normalized and dose-weighted using MotionCor2 (Zheng et al., 2017). Defocus values were determined using GCTF (Zhang, 2016). Particles were automatically picked with Gautomatch using the template-free mode (Gaussian blob with 220 Å diameter), imported to RELION-3 (Zivanov et al., 2018) and extracted in 224 pixel-sized boxes. Extracted particles were applied to 2D classification routine in RELION-3 to remove contaminations. 1,873,975 particles were selected and after removing low quality classes, initial 3D reconstruction was performed

using cryoSPARC (Punjani et al., 2017). Using the initial model, 5 batches of 3D classification were performed, yielding several models of a closed talin structure with different completeness of densities. Particles of the most complete model were combined, further aligned and classified. 30,438 particles were selected for the final 3D refinement, yielding a final map with a global resolution of 6.2 Å with up to 5.5 Å resolution in the core of talin using the RELION post-processing routine, using the gold-standard Fourier shell correction (FCS) = 0.143 criterion. In the final map, the R3 domain was only partially resolved. To visualize the R3 domain, flexible densities were computationally subtracted from individual particles using available scheme from RELION-3, and as previously described (Bai et al., 2015), facilitating the focused 3D classification of the core density R1-R10. The particle information and the alignment parameters of the 3D class with the most prominent density of R3 were applied to the original particles that contain the flexible densities (FERM domain and R11-C) and the final map with the R3 domain was obtained. This map was used for the assignment of the R3 domain. Finally, to assess the flexibility of the autoinhibition area in the talin structure, 3D classification was performed to the 750,432 particles obtained from the initial stage of the 3D classification. It was observed that the parts corresponding to R11-R13 exhibited a weaker density compared to the core part (R1-R10) of the structure, detecting high levels of flexibility. Overall, the analysis indicated that the packing of talin-FL is sensitive to its environment, which agrees well with its conformational change observed in our biochemical analysis as well as its cellular function. The graphical summary is depicted in Figure S1.

Molecular dynamics for flexible fitting

For each of the rod fragments (R1-R13) and the FERM domains, crystal and NMR structures are available. The corresponding PDB entries are 3ivf (FERM domain), 1sj8 (rod domains R1 and R2), 2l7a (R3), 2lqg (R4), 2l10 (R6), 2l7n (R5) 5ic1 (R7, R8, R9), 2kvp (R10), 3dyj (R11, R12), 2jsw (R13). Initially, the structures containing multiple domains (PDB: 3ivf, 1sj8 and 5ic1) were computationally divided into individual domains. These individual domain structures served as building blocks to build a model of the entire autoinhibited structure of talin (Figure S3).

The R1 rod domain has an asymmetric shape and only one unique well-fitted placement and orientation of this structure in the density could be identified by rigid-body fitting. The C-terminus of the fitted R1 model reaches into a neighboring helical bundle density in the cryo-EM map, which fitted well with the R2 model. The available structure of R1-R2 complex (PDB: 1SJ8) was independently fitted using the colores program of the Situs package (Chacón and Wriggers, 2002) showing that they matched to each other. This fitting served as a first anchor segment. The resolution of the density was sufficient to clearly distinguish between 4-helix and 5-helix bundle segments in the density. R7 and R8 were readily identified due to the inter-winded helical bundle feature of R7 within R8. Together with the constraint on the maximum linker length to covalently connect consecutive rod-domains it was possible to define placements and also orientations of the subsequent rod domains (R3-R13) in order to fit to the density and at the same time, to allow covalent connection to the previous and subsequent rod-domains. Placements that sterically did not allow connection of consecutive fragments to form a fully connected talin chain were eliminated. Finally, remaining densities, which did not represent a helical bundle arrangement, were assessed. These remaining densities consisted of two globular entities that were identified as F2 and F3 domains due to their secondary structures features. Overall, the fitting was performed independent of any available structural models showing the inter-domain connections. However, our placements brought the F3 segment in close binding vicinity to the R9 rod-domain. The placement coincided with the crystal structure of F2-F3 in complex with R9 (PDB 4f7g) (within a root-mean square deviation (RMSD) < 0.8 Å).

The resolution of the cyro-EM reconstruction of 6.2 Å together with the sterical constraints to covalently connect domains with smaller linker segments readily allowed the identification of the unique topology for the full chain. However, no cryo-EM densities for the FERM F0 and F1 domains and the DD domain were identified and these parts were not included during model building. Finally, a full covalently connected chain was formed by connecting N- and C-termini of consecutive rod fragments using the Leap module of the Amber16 package (Salomon-Ferrer et al., 2013) in combination with the ff14SB force field (Maier et al., 2015). The disordered connection between FERM F3 and R1 was not included and the F2 and F3 domains were treated as separate proteins not covalently connected to the rod fragments.

The emap/sander module of the Amber16 package was used to perform a flexible fitting and sterical force field optimization (based on the ff14SB force field). In order to keep the structure of each individual template structure (R1-R13 and F2 and F3) close to the corresponding experimental crystal structure distance restraints between backbone atoms within each fragment were included. These restraints kept the secondary structure and the arrangement of secondary structures in each domain to within RMSD < 1 Å from the corresponding experimental domain reference structures. Connecting loops and side chains were nevertheless fully mobile during flexible fitting. The full start structure was first energy minimized (5000 steps) followed by a Molecular Dynamics (MD) simulation at 300 K (0.5 ns) until no further shift of the mean structure was observed followed by another round of energy minimization. The model was then subjected to manual building and correction in COOT (Emsley et al., 2010) and real-space refinement in PHENIX (Afonine et al., 2018). The final structure fitted well to the cryo-EM density with a correlation coefficient around the model (CC_{mask}) of 0.81 without outliers in the Ramachandran plot (Table S1).

Estimation of interaction energies

The interaction energy between selected pairs of talin fragments (enthalpy) was calculated using the MMPBSA (Molecular Mechanics Poisson Boltzmann Surface Area) approach as implemented in the Amber18 package (Onufriev et al., 2000; Salomon-Ferrer et al., 2013). Pairs of talin subdomains were extracted from the compact talin autoinhibited structure in the same arrangement as observed

in the full structure. For each case an ensemble of 250 conformations was generated using short MD simulation (0.1 ns, 300 K) keeping the backbone strongly restraint to the starting placement (allowing shifts < 0.1 Å). The mean domain-domain interaction energy was calculated using the MMPBSA method. It accounts for changes in electrostatic Coulomb interactions, changes in electrostatic solvation (reaction field with the aqueous environment), changes in mean van-der-Waals interactions and nonpolar (hydrophobic) contributions that depend on the buried surface area upon complex formation. In the MMPBSA approach, the change in electrostatic reaction field contributions is calculated by solving the finite-difference Poisson-Boltzmann equation for each structure. The energy of interaction was estimated by subtracting the contributions of each partner from the result of the domain-domain complex for each case. Calculations were performed at a monovalent salt concentration of 0.15 M. We note that the calculated interaction energies represent enthalpic contributions and do not include the entropic penalties of restricting the large ensemble of open and flexible conformations of talin to a small ensemble of compact conformations seen in the autoinhibited state.

F-Actin co-sedimentation assay

Actin was purchased from Hypermol, Germany. Actin was polymerized in 10 mM Tris pH 7.5, 50 mM KCl, 2 mM $MgCl_2$, 0.2 mM $CaCl_2$, 0.2 mM ATP, 0.5 mM DTT for 20 min at RT. Buffer exchange of the samples was performed using Zeba Spin desalting columns (Thermo Scientific). The buffer for all constructs was 20 mM Tris pH 7.5, 75 mM KCl. 2.5 μM talin fragments were incubated with 2.5 μM F-actin for 15 min at RT. The mixture was then ultra-centrifuged at 175 000 x g (TL-100 Ultracentrifuge, Beckmann) for 20 minutes at RT. Pellets were re-suspended to comparable volumes as supernatants with 1x SDS buffer. 6x SDS buffer was added to the supernatant and 10 μl of samples were run on SDS-page and quantified using FIJI (Schindelin et al., 2012).

Analytical size-exclusion chromatography

For analytical size-exclusion chromatography, the buffer exchange of the sample was performed using Zeba Spin desalting columns (Thermo Scientific) to 20 mM HEPES pH 7.5, 75 or 500 mM KCl, and 10 μM of samples were injected to either an analytical Superdex 200i 3.2/300 (for the reconstitutions of R1-C, R1-R3, R4-R8 and R4-R8 and V-head) or Superose 6i 3.2/300 (all other constructs) on an ÄKTAmicro system (GE Healthcare). Fractions were collected, mixed with 6x SDS sample buffer and 10 μl were run on SDS-PAGE.

Dynamic Light-Scattering (DLS)

For measurements of hydrodynamic radius changes, talin-FL, talin N-R11 and talin N-R12 were initially prepared in 20 mM HEPES pH 7.5, 75 mM KCl, 0.5 mM EDTA, 0.5 mM β-Mercaptoethanol. Further, the samples were diluted to a final concentration of 0.3 mg/ml and final KCl concentrations of 75 – 500 mM (75/100/125/150/175/200/225/250/300/350/400/450/500 mM KCl) in the same buffer in 30 μl wells in a 384-well plate. DLS measurements were performed with a Dynapro Platereader-II Dynamic Light Scattering instrument (Wyatt Technology Corporation) at 20°C. Samples were independently prepared in triplicates and 20 measurement points per well were taken. The data was analyzed in Dynamic 7.8.1.3 (Wyatt Technology Corporation) and plotted with PRISM (GraphPad). The fitting of the curve was performed using a nonlinear regression fit with a sigmoidal curve.

Size-Exclusion Chromatography Coupled with Multi-Angle Light-Scattering (SEC-MALS)

To test the molecular weight of the protein complexes, talin-FL and talin truncations as well as the mixtures of talin and vinculin (1:1 ratio) were prepared in buffer containing 20 mM HEPES, pH 7.5, 75 or 500 mM KCl, 0.5 mM EDTA at 3 mg/ml concentration and 20 μl were run on a Superdex 200 5/150 GL column on an ÄKTAmicro system (GE Healthcare) coupled to a Viscotek TDA302 detector (Malvern, Herrenberg, Germany) in the same buffer. Bovine serum albumin was used as a standard and the refractive index increment (dn/dc) was set to 0.180 ml/g for calculations. Data was analyzed using the OmniSEC 4.5 software (Malvern) and plotted with PRISM (GraphPad).

QUANTIFICATION AND STATISTICAL ANALYSIS

Quantification and statistical analysis related to EM data are integral parts of algorithms and software used.

For DLS analysis, the experiments were performed 3 times independently. The results were averaged and the error bars represent the standard deviations. For the fitting, nonlinear regression fit, sigmoidal curve fitting was applied using the software PRISM (GraphPad).

For F-actin analysis shown in Figure 6, the experiments were performed at least 3 times independently. The talin-FL band was run on the same SDS-PAGE gel as an internal control to standardize the variability of the contrast caused by staining conditions of each SDS-PAGE gels. Therefore, relative quantified values compared to the talin-FL band were used for the analysis. These values were averaged and standard deviations were obtained. Unpaired t-test was used to assess statistical significance.

DATA AND CODE AVAILABILITY

The cryo-EM map of human talin1 was deposited in the EMDB database with accession code EMD-4772. The flexibly fitted atomic model was deposited in the PDB with accession code 6R9T.

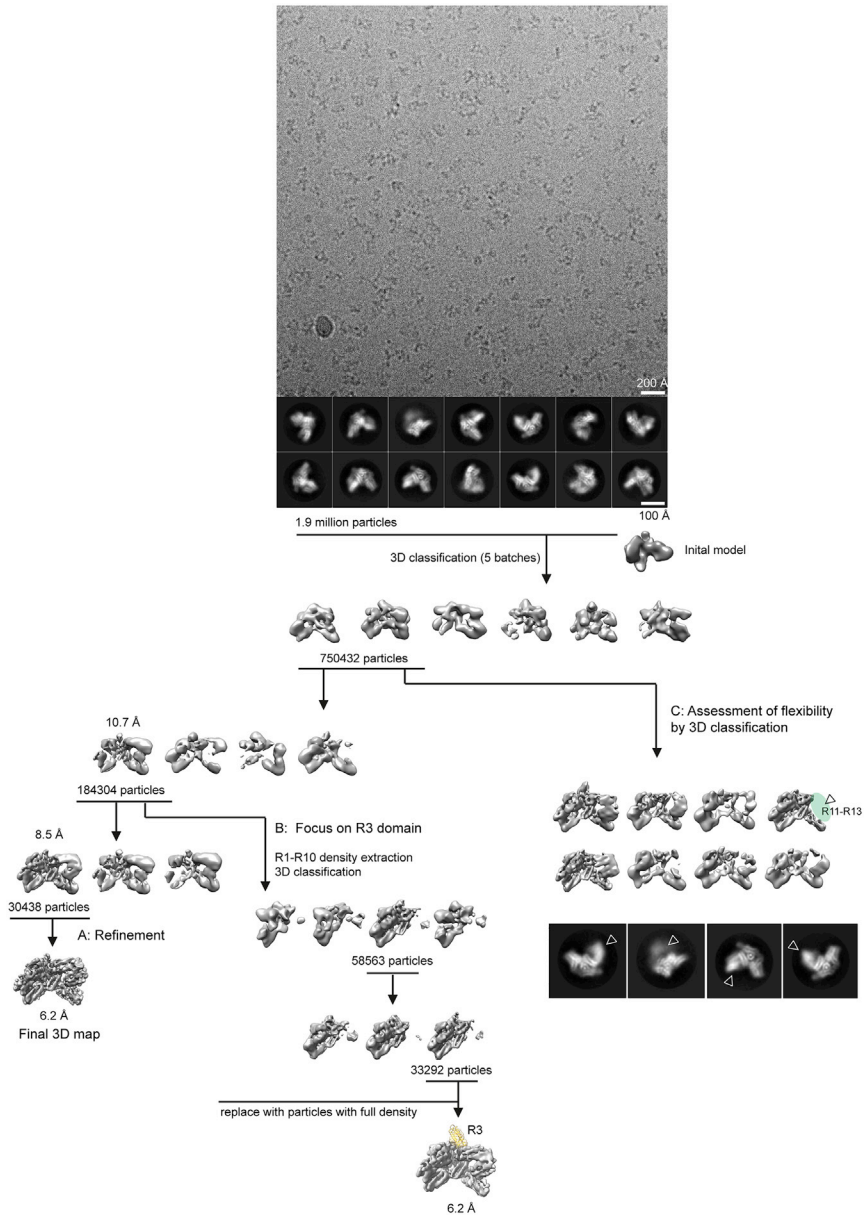

Figure S1. Summary of Cryo-EM Data Processing, Related to Figure 1

Top: Representative cryo-EM image of talin-FL at 75 mM salt with representative 2D averages. Bottom: Graphical scheme of image processing. 1.9 million particles were selected out of 2D classifications. Further 3D classifications and refinement facilitated the final map generation (A – left). To visualize the R3 domain, the core density (R1-R10) was computationally extracted and focused 3D classification of the core density was performed. At the final step of the processing, the alignment parameters were applied to the original particles to visualize the full density (B – center). Yellow density fitted with an available structural model of R3. To assess the flexibility of the autoinhibition pocket consisting of the interface between FERM domain F2-F3 and R12-R13 (lid), extensive 3D classifications were performed, yielding a visualization of the flexible densities of R11-R13 (C – right).

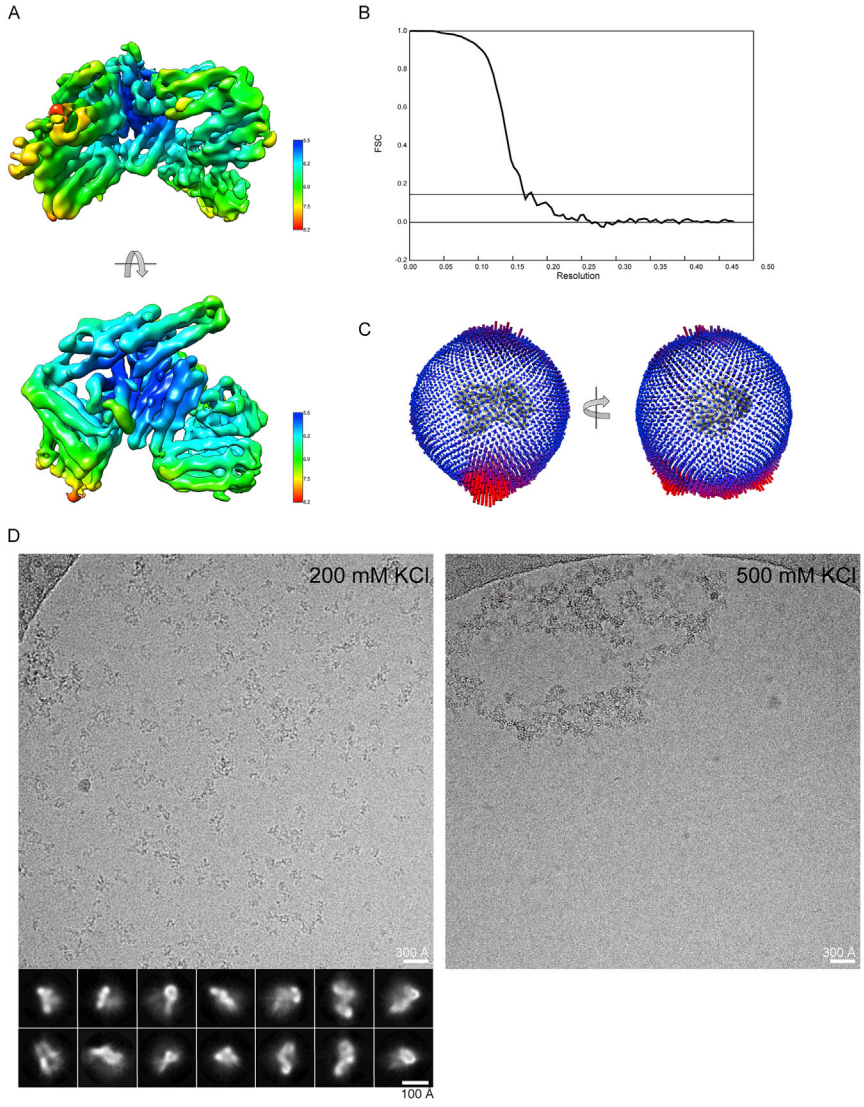

Figure S2. Quality Control of Cryo-EM Data Processing, Related to Figure 1

A: Local resolution map of the talin-FL structure, showing a resolution range between 5.5 Å and 7.9 Å. B: The Fourier shell correlation (FSC) curve of the talin-FL structure showing a global resolution of 6.2 Å. The additional line indicates a FSC of 0.143 C: Angular distributions of the particle orientations that were incorporated into the final 3D reconstruction. D: Cryo-EM images of talin-FL in the presence of 200 mM KCl and 500 mM KCl, showing aggregations presumably due to the talin opening at 500 mM KCl. 2D classifications of talin-FL at 200 mM KCl reveal less robust averages indicating higher structural heterogeneity.

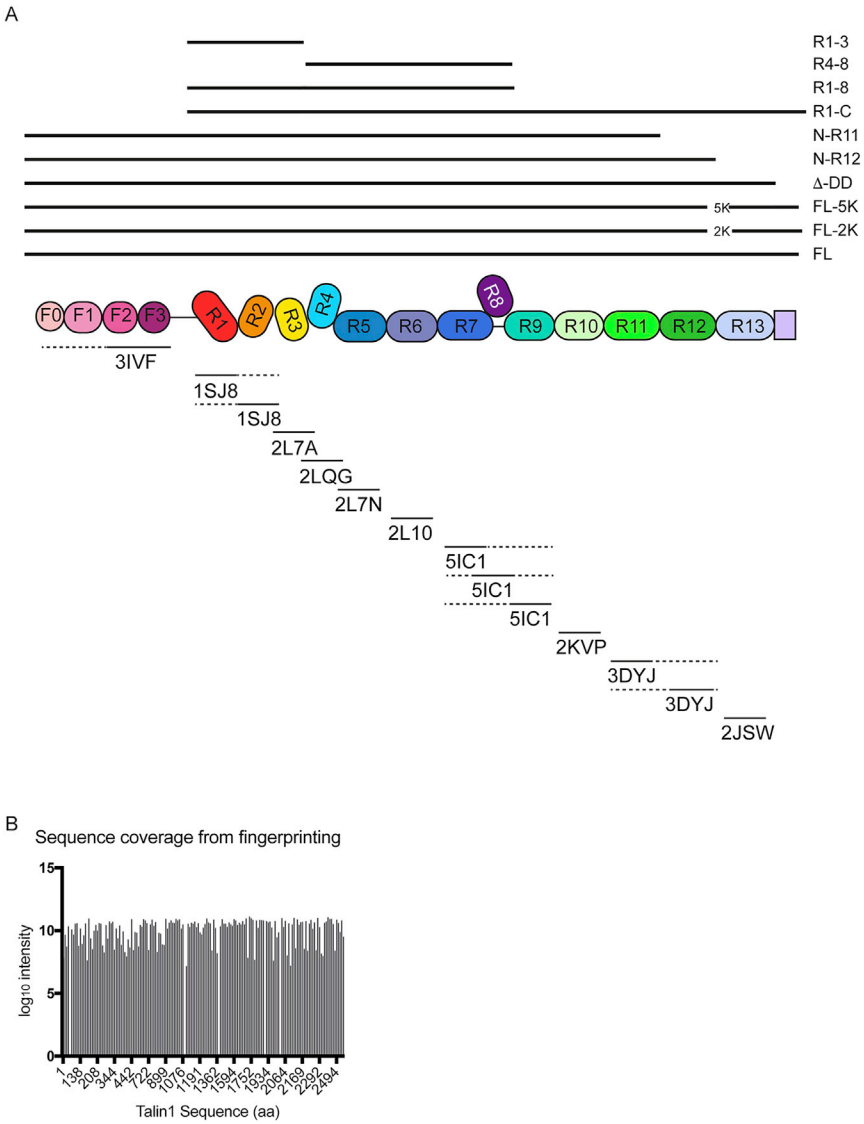

Figure S3. Talin Fragments Used in This Study and Sequencing Information of Talin-FL, Related to Figure 1

A: Scheme of talin fragments used in this study (top) and the structures (PDB codes) that were used as building blocks for the fitting and molecular modelling. For PDBs 3IVF, 1SJ8, 5IC1 and 3DYJ, individual domains are computationally extracted and used independently (see also STAR methods). 2K denotes charge-reversal double mutation E2288K, E2294K and 5K denotes mutations E2288K, E2294K, D2297K, E2299K, D2300K). B: Peptide detection of talin-FL by mass spectrometry. The entire sequence of talin (1-2541) is covered, showing no indication of spontaneous cleavage.

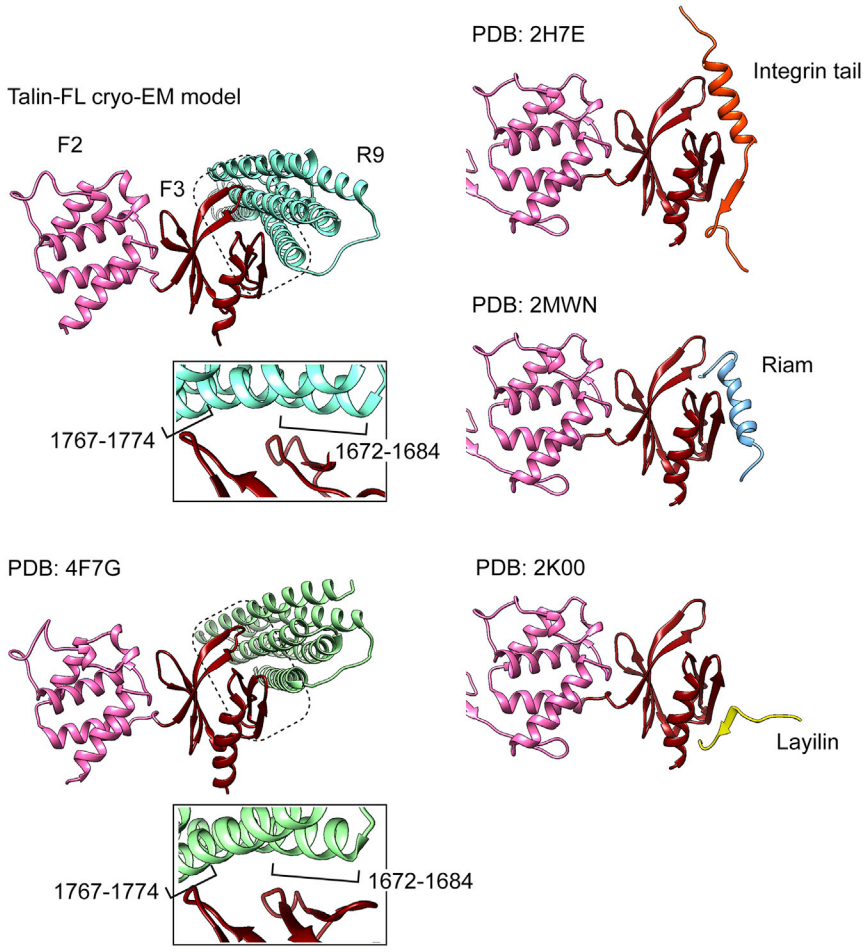

Figure S4. Talin F3-Rod Binding Surfaces Obtained from Our Cryo-EM Map in Comparison to Available Structures, Related to Figure 1

Top-left: Our cryo-EM model of the F3-rod binding surface. Bottom-left: crystal structure (PDB: 4F7G) of truncated F2-F3 and R9. Right: Examples of structures that bind to the talin F3-rod binding surface. From top to bottom: PDB: 4F7G superimposed to 2H7E (Integrin tail), 2MWN (RIAM), and 2K00 (Layilin).

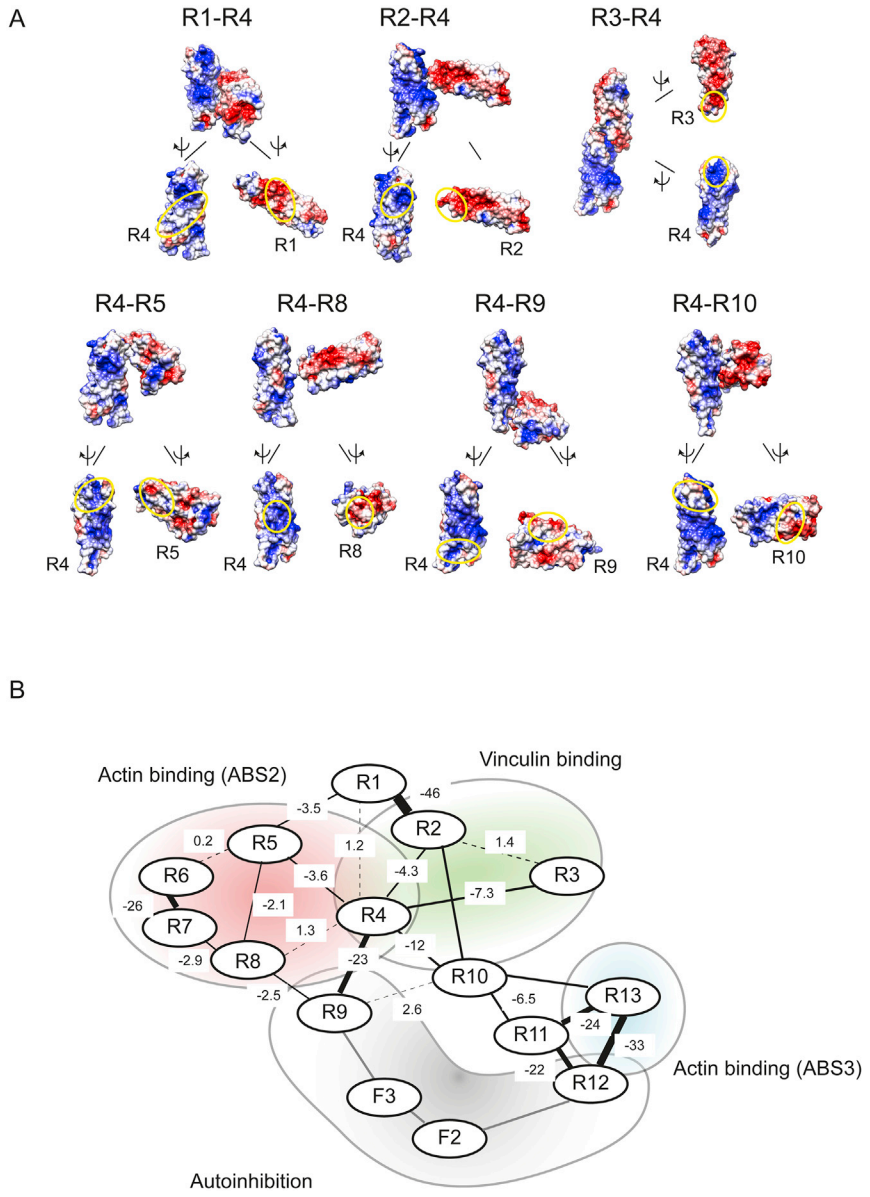

Figure S5. Talin Inter-Domain Interactions, Related to Figures 1 and 4

A: Electrostatic surface potential of individual rod domains surrounding R4 and forming the autoinhibition core. Sites contacting each other are indicated with yellow circles. B: Interaction energies calculated by restraint molecular dynamics simulations for major interaction surfaces in the presence of 150 mM salt. Units: kCal/mol. We note that the calculated interaction energies represent enthalpic contributions and do not include the entropic penalties of restricting the large ensemble of open and flexible conformations of talin to a small ensemble of compact conformations seen in the autoinhibited state.

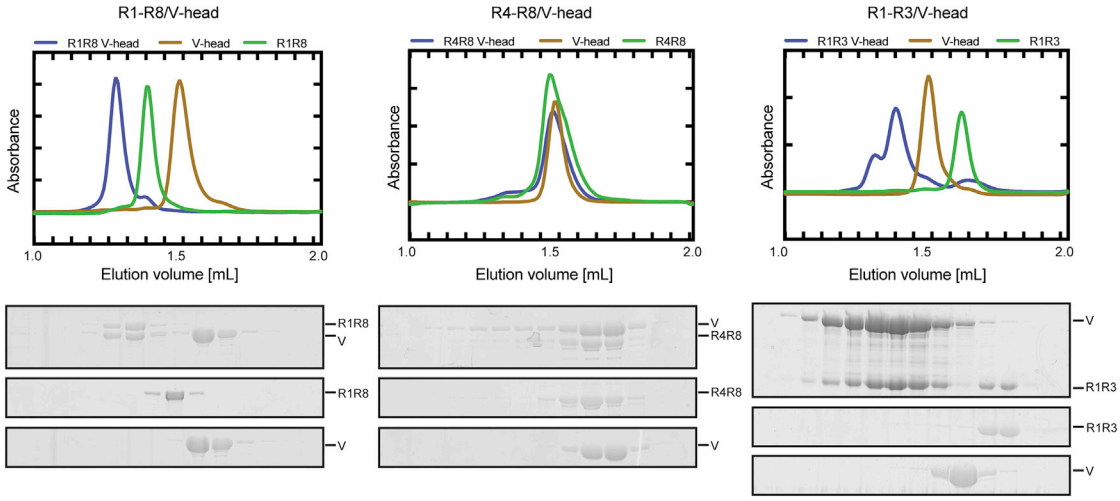

Figure S6. SEC Reconstitution Assay of Various Talin Rod Domains and the Vinculin Head (V-Head) at 75 mM Salt, Related to Figure 5

The SDS-PAGE analysis corresponds to the profile of the protein mixtures (top), talin control constructs (center), and vinculin head control (bottom), respectively.

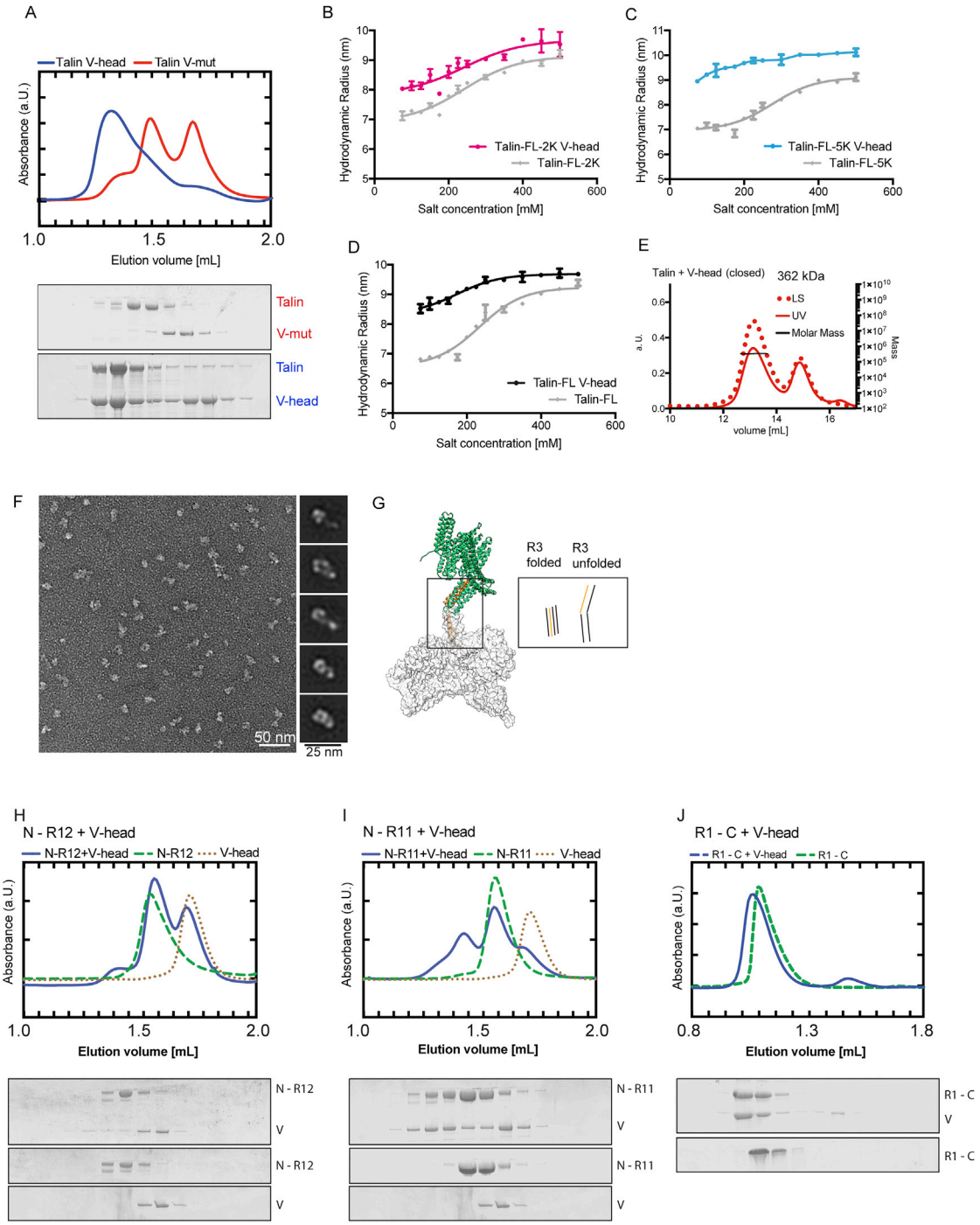

Figure S7. Conformational Change of Talin in Complex with V-Head, Related to Figures 5 and 6

A: Size-exclusion chromatography (SEC) profile of talin and vinculin constructs. Reconstitution assays of talin (open conformation) and V-head as well as V-mut were performed at 500 mM salt, and then the complex was assessed by changing the salt concentration to 75 mM. V-head stays in complex with talin (blue), while V-mut dissociates from talin (red). B-D: DLS measurements of the hydrodynamic radius of the reconstituted talin constructs (talin-FL, talin-FL-2K and talin-FL-5K) in complex with V-head under various salt concentrations. In comparison to talin-FL constructs alone (shown in grey), the increased size of the sample is observed showing complex formation. A conformational change of talin-V-head complex upon the change of salt concentration is also observed. For the case of talin-FL-5K in complex with V-head, the profile did not fit to a two-state model. E: SEC-multi-angle light-scattering profile of the talin (75mM salt, closed) -V-head complex showed a molecular weight of 362 kDa, indicating a 1:1 stoichiometry. LS: light scattering, normalized, UV: absorbance F: Negative-stain EM image of the talin-vinculin head complex in closed talin and two-dimensional averages (right), showing a long protrusion from the main globular density. G: Molecular modeling of our talin structure (white) with R3 unfolded (yellow) to accommodate the vinculin head density (green). The model was created by combining our cryo-EM talin-FL

(legend continued on next page)

structure (white) with available structures of a part of the V-head (a.a. 1–258) complexed with talin peptide (a.a. 1944–1969) (PDB: 1RKC, yellow) and the vinculin head (a.a. 259–843) extracted from full-length vinculin (PDB: 1TR2, green). H-J: SEC profiles of various talin truncation constructs with V-head at 75 mM salt, showing that the complex formation of talin and V-head occurs only with N-R11 (I) and R1-C (J). N-R12 containing the R12 (lid) did not form a complex with V-head (H). In the reconstitution assay of R1-C + V-head, a Superdex S200 column was used while a Superose 6 was used for the other assays. The control runs for V-head come from the same experiment and the corresponding profile and SDS-PAGE are shown twice for comparison. Error bars show standard deviations.